



Available online at www.sciencedirect.com

ScienceDirect

Geochimica et Cosmochimica Acta 278 (2020) 177–198

Geochimica et
Cosmochimica
Acta

www.elsevier.com/locate/gca

Dating post-Archean lithospheric mantle: Insights from Re-Os and Lu-Hf isotopic systematics of the Cameroon Volcanic Line peridotites

Jingao Liu ^{a,b,*}, D. Graham Pearson ^b, Qiao Shu ^{c,b,h}, Haraldur Sigurdsson ^d,
Emilie Thomassot ^e, Olivier Alard ^{f,g}

^a State Key Laboratory of Geological Processes and Mineral Resources, China University of Geosciences (Beijing), Beijing 100083, China

^b Department of Earth and Atmospheric Sciences, University of Alberta, Edmonton, Alberta T6G 2E3, Canada

^c State Key Laboratory of Ore Deposit Geochemistry, Institute of Geochemistry, Chinese Academy of Sciences, Guiyang 550081, China

^d Graduate School of Oceanography, University of Rhode Island, Kingston 02881, United States

^e ETH-Zürich Institute for Geochemistry and Petrology, Clausiusstrasse, 258092 Zürich, Switzerland

^f ARC Centre of Excellence for Core to Crust Fluid Systems and GEMOC National Key Centre, Dept of Earth and Planetary Sciences, Macquarie University, NSW 2109, Australia

^g Géosciences Montpellier, UMR5243, CNRS & Université de Montpellier, 34095 Montpellier, France

^h CAS Center for Excellence in Comparative Planetology, China

Received 31 January 2019; accepted in revised form 3 July 2019; available online 12 July 2019

Abstract

Highly depleted Archean peridotites have proven very amenable to Re-Os model age dating. In contrast, due to the increasing heterogeneity of mantle Os isotope compositions with time, the Re-Os system has not been as effective in dating post-Archean peridotites. The timing of depletion and accretion of post-Archean lithospheric mantle around cratons is important to understand within the context of the evolution of the continents. In an attempt to precisely date post-Archean peridotite xenoliths, we present a study of the petrology, mineralogy and geochemistry, including whole-rock Re-Os isotopes, highly siderophile elements and clinopyroxene-orthopyroxene Sr-Nd-Hf isotopes of peridotite xenoliths from Lake Nyos in the Cameroon Volcanic Line (CVL). Eight Nyos peridotite xenoliths, all fresh spinel lherzolites, are characterized by low to moderate olivine Fo contents (88.9–91.2) and low spinel Cr# (8.4–19.3), together with moderate to high whole-rock Al₂O₃ contents (2.0–3.7%). These chemical characteristics indicate that they are mantle residues of a few percent to <20% partial melting. However, trace element patterns of both clinopyroxene and orthopyroxene are not a pristine reflection of melt depletion but instead show various extents of evidence of metasomatic enrichment. Some of the samples contain orthopyroxene with ¹⁴³Nd/¹⁴⁴Nd lower than its coexisting clinopyroxene, which is best explained by recent short-timescale alteration, most likely by infiltration of the host basalt. Because of these metasomatic effects, the Sr-Nd isotope systematics in pyroxenes cannot sufficiently reflect melt depletion signatures. Unlike Sr-Nd isotopes, the Lu-Hf isotope system is less sensitive to recent metasomatic overprinting. Given that orthopyroxene hosts up to 33% of the Lu and 14% of the Hf in the whole rock budget of these rocks and has ¹⁷⁶Hf/¹⁷⁷Hf similar to, or higher than, coexisting clinopyroxene, it is necessary to reconstruct a whole-rock Lu-Hf isochron in order to constrain the melt depletion age of peridotites. The reconstructed Nyos Lu-Hf isochron from ortho- and clinopyroxenes gives an age of 2.01 ± 0.18 Ga (1σ), and when olivine and spinel are considered, is 1.82 ± 0.14 Ga (1σ). Both ages are identical within error, and they are within error of the alumina-¹⁸⁷Os/¹⁸⁸Os pseudo-isochron ages (1.2–2.4 Ga) produced on the peridotites from Lake Nyos, consistent with their oldest rhenium depletion Os

* Corresponding author at: State Key Laboratory of Geological Processes and Mineral Resources, China University of Geosciences (Beijing), Beijing 100083, China.

E-mail address: jingao@cugb.edu.cn (J. Liu).

model ages (2.0 Ga). We conclude that the Nyos peridotites, and the lithospheric mantle that they represent, were formed at ~2.0 Ga, indicating that the reconstructed whole-rock Lu-Hf isotope system can be a powerful radiometric dating tool that is complementary to and in some instances, more precise than the Re-Os isotope system in dating well-preserved post-Archean peridotites. The recognition of ~2.0 Ga subcontinental lithospheric mantle (SCLM) in the Nyos area suggests that the Nyos region was assembled as a Paleoproterozoic block, or that it represents fragments of the SCLM from the nearby Paleoproterozoic domain juxtaposed through collisional emplacement during the Pan African Orogeny. With regards to the origin of the CVL, our data reveal that the Hf isotopic compositions of the Nyos peridotites are too radiogenic to be the main source of the CVL basalts.

© 2019 Elsevier Ltd. All rights reserved.

Keywords: Sr-Nd-Hf; Highly siderophile elements; Re-Os isotopes; Peridotite dating; Cameroon Volcanic Line

1. INTRODUCTION

Partial melting of the mantle generates melts and residues to form crust and underlying lithospheric mantle that constitute the lithosphere on Earth. However, the genetic relationship of continental crust and underlying lithospheric mantle is unclear in most tectonic settings, because of the compositional and geochronological decoupling of crust and lithospheric mantle (e.g., Lee et al., 2000; Peslier et al., 2000; Gao et al., 2002; Luguet et al., 2009; Liu et al., 2015). One key issue is the difficulty of precisely dating mantle peridotites that comprise the major component of the underlying lithospheric mantle (Rudnick and Walker, 2009, and references therein). Residual peridotites are depleted in lithophile-element-based radioactive isotope systems (e.g., Rb-Sr, Sm-Nd, U-Th-Pb) that are easily modified or reset by subsequent overprinting or thermal events (e.g., Carlson and Irving, 1994; Pearson and Nowell, 2002), thus, these isotope systems are not suited to extracting the melt depletion age of the residue. In contrast, the chalcophile-siderophile Re-Os isotope system has long been shown to be more effective at dating peridotites than lithophile element based isotopic systems due to the contrasting geochemical behavior of Re and Os (i.e., Re is moderately incompatible while Os is compatible during mantle melting) and their greater robustness to perturbation from secondary overprinting (e.g., Walker et al., 1989; Carlson and Irving, 1994; Pearson et al., 1995; Reisberg and Lorand, 1995). Given that Re often suffers recent modification particularly for those peridotite xenoliths erupted by alkali lava (e.g., Irvine et al., 2001), undisturbed Re-Os isochron systematics are rarely observed in peridotites. To circumvent this issue, Os model ages are usually utilized — T_{MA} being calculated in a way similar to a crustal Nd model age, assuming it remains a closed system evolving from the mantle evolution line, while T_{RD} is calculated assuming that no Re remains in the residue evolving from the mantle reference line and thus is a minimum estimate of mantle partial melting (Walker et al., 1989; Pearson et al., 1995). The combination of T_{MA} and T_{RD} has been successful in constraining the formation age of cratonic refractory peridotites demonstrating its longevity and its long-term coupling with its overlying crust (e.g., Carlson et al., 1999; Pearson et al., 2004; Pearson and Wittig, 2014 and references therein).

Despite this success, Os model ages yield much larger uncertainties in dating post-Archean peridotites mainly due to their typically lower degrees of partial melting, the mobility of more Re and the greater diversity of Os isotope composition in Phanerozoic-Proterozoic versus Archean mantle (e.g., Pearson et al., 2007; Rudnick and Walker, 2009; Luguet and Pearson, 2019). To address the mobility of Re, aluminum (and other immobile melt depletion indices, for example, Lu, Yb) has been applied as a proxy of Re/Os ratio to construct a pseudo-isochron in order to calculate the initial Os isotopic ratio that is subsequently used to estimate the melt depletion age (e.g., Reisberg and Lorand, 1995; Handler et al., 1997). Nevertheless, this is a relatively blunt tool complicated by the fact that metasomatism could alter melt depletion indices to some extent. In addition, the exact point of complete Re extraction determined by melt depletion indices may vary from one suite to another. But the largest source of error is likely that the mantle evolution reference line is not well defined, including various chondritic mantle (ranging from carbonaceous (Walker et al., 1989) to ordinary (Pearson and Wittig, 2008) composition) and primitive upper mantle estimates (Meisel et al., 2001). Different mantle evolutionary models could generate a discrepancy of ca. 0.2 Ga (Pearson et al., 2007; Rudnick and Walker, 2009). All of these factors make the Re-Os isotope system not ideally suited to dating post-Archean peridotites and complementary systems should be sought. Recently, unlike the Sr-Nd-Pb isotope systems, the Lu-Hf isotope system of clinopyroxene has been demonstrated to show its success as a complementary tool to the Re-Os isotope system in dating spinel-facies mantle peridotites (e.g., Schmidberger et al., 2002; Pearson and Nowell, 2003; Carlson et al., 2004; Wittig et al., 2006; Bizimis et al., 2004; Liu et al., 2012; Doucet et al., 2015; Ackerman et al., 2016). However, the contribution of orthopyroxene is either ignored or arbitrarily estimated in these studies, but should be considered (Stracke et al., 2011; Byerly and Lassiter, 2015), as orthopyroxene has 3 to 4 times higher Lu/Hf ratios than coexisting clinopyroxene and contains significant proportions of both elements, e.g., up to 40% of the whole rock budget for Hf and up to 60% for Lu (Liu et al., 2012; Byerly and Lassiter, 2015). Moreover, although the low Lu concentrations in olivine are approximately one tenth of the concentrations of coexisting orthopyroxene, its high modal abundance

indicates that olivine hosts several percent of the total Lu inventory and is characterized by higher Lu/Hf ratios (e.g., Byerly and Lassiter, 2015). Previous work on the Lu-Hf isotope system of garnets derived from clinopyroxene-free peridotites showed that the Lu-Hf isochron ages derived from subcalcic garnets (not existing with clinopyroxenes) alone are systematically younger because of the coexistence of orthopyroxene in these rocks (Lazarov et al., 2009; Shu et al., 2013). Likewise, the effects from orthopyroxene and olivine on the Lu-Hf isotope system of clinopyroxene in garnet-free peridotites should be considered. Here we apply the Re-Os and Lu-Hf isotope system to a suite of fresh moderately depleted post-Archean peridotites to evaluate the effectiveness of both systems in providing age information pertinent to their genesis.

The Cameroon Volcanic Line (CVL) is composed of a chain of Cenozoic volcanoes formed both on the Atlantic oceanic floor and the continental crust of the African plate (Fig. 1a). The origin and petrogenesis of this unique geological feature have received considerable attention from geochemical, structural, geophysical and geochronological perspectives (Assah et al., 2015, and references therein). It is concluded that the CVL most likely results from reactivation of lithospheric cracks (shear zones) tapping sub-lithospheric mantle with little to moderate reaction with the lithospheric mantle (Meyers et al., 1998; Déruelle et al., 2007; Assah et al., 2015), rather than resulting from

melting of a deep mantle plume (Lee et al., 1994). By contrast, the subcontinental lithospheric mantle (SCLM) sampled by peridotite xenoliths in several localities of the CVL lavas remains poorly studied (e.g., Lee et al., 1996; Princivalle et al., 2000; Tamen et al., 2015; Teitchou et al., 2007; Wandji et al., 2009; Matsukage and Oya, 2010; Temdjim, 2012; Pintér et al., 2015; Liu et al., 2017). Most previous studies were focused on peridotite petrology, mineralogy, and elemental geochemistry as well as thermal histories to unravel melt depletion and metasomatic processes, but only a few studies were devoted to dating the melt depletion and/or metasomatic evolution of the SCLM (Lee et al., 1996; Liu et al., 2017). This significantly limits our understanding of formation and evolution of the SCLM in the context of the geodynamics of this region, and also affects the evaluation of the role of the SCLM in the formation of basaltic lavas. The published Late Proterozoic Nd-depleted mantle ages of minimally metasomatized peridotites from the continental sector of the CVL were interpreted to represent their formation age, whereas the metasomatized peridotites gave Mesozoic Nd model ages interpreted to reflect Mesozoic enrichment related to the mantle sources for the basaltic host lavas (Lee et al., 1996). Recently, Re-Os isotope work on the peridotites from Lake Nyos was interpreted as reflecting an Archean formation age of ~2.6 Ga based on a $^{187}\text{Os}/^{188}\text{Os}$ -Al₂O₃ pseudoisochron (Liu et al., 2017). This either indicates the extreme heterogeneity of the SCLM beneath the CVL, or

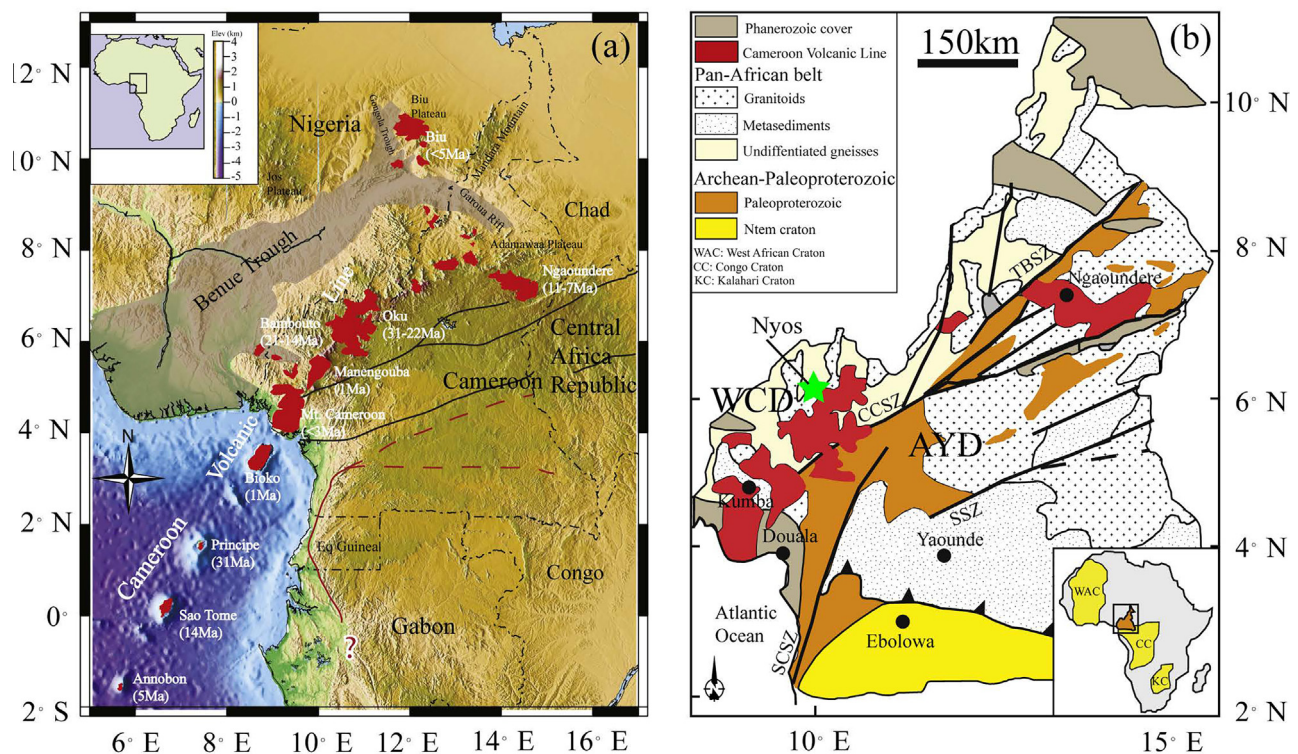


Fig. 1. (a) Geographic map of the Cameroon Volcanic Line with locations of major volcanic centers (modified after Reusch et al., 2010). (b) Schematic geologic map of Cameroon showing the major lithospheric units (modified after Toteu et al., 2001; Liu et al., 2017). Abbreviation: WCD – Western Cameroon Domain; AYD – Adamawa-Yadé Domain; SCSZ – South Cameroon Shear Zone; CCSZ – Central Cameroon Shear Zone; TBSZ: Tcholliré-Banyo Shear Zone; SSZ: Sanaga Shear Zones.

reflects large uncertainties in the radiometric dating. A corroborating chronologic determination is, therefore, needed.

Here we present a study of petrology, mineralogy, and geochemistry, as well as whole-rock Re-Os isotopes, highly siderophile elements (HSE here including Re, Os, Ir, Ru, Pt, and Pd) and clinopyroxene-orthopyroxene Sr-Nd-Hf isotopes of peridotite xenoliths from Lake Nyos, Mt. Oku in the Cameroon Volcanic Line. This comprehensive work provides a good opportunity to address the issue of dating post-Archean peridotites raised above. On the basis of this, we will discuss the geodynamic implications of the SCLM and the relationship with its overlying crust in the framework of the Pan-African orogenic belt and amalgamation of the African cratons. In addition, the contribution of the SCLM in the petrogenesis of the CVL basaltic lavas will be evaluated.

2. GEOLOGIC BACKGROUND AND SAMPLE DESCRIPTIONS

Comprehensive field, petrological, structural, geochemical and geochronological studies show that the Central African Fold Belt of Cameroon is composed of several domains including Paleoproterozoic gneissic basement, Mesoproterozoic to Neoproterozoic volcano-sedimentary basins (e.g., Yaoundé and Poli sedimentary basin or meta-sedimentary series), and voluminous Pan African granitoids (Fig. 1b; Toteu et al., 2001). Pre-drift reconstructions of the supercontinent Pangea show that the Precambrian basement of Cameroon was attached to that of NE Brazil. These two regions were part of the major ~600 Ma Pan African-Brasiliano orogenic belt that extended from NE Brazil through central Africa to much of Saharan Africa (Toteu et al., 2001, and references therein). This belt marked the assembly of West Gondwana when the West African and Congo-São Francisco cratons collided (Trompette, 1994), while the fusion of the Congo and São Francisco cratons occurred earlier, sutured partially by the 2.1 Ga Nyong series metamorphic complex in SW Cameroon resulting from the ca. 2.1 Ga Eburnian-Transamazonian orogeny (Ledru et al., 1994; Tanco Njiosseu et al., 2005). The 2.1 Ga Eburnian orogeny may have resulted in the formation of the Paleoproterozoic Adamawa-Yadé Domain mainly through the reworking or melting of Archean crust on the northern edge of the Congo Craton, and this Paleoproterozoic block may not have extended northward beyond the Central Cameroon-Tcholliré-Banyo shear zones (Fig. 1b; Toteu et al., 2001, 2004). The Pan African granitoids in this region were formed mostly by reworking or melting of 2.1 Ga Eburnian crust with limited juvenile inputs through the Pan African orogeny. However, the Yaoundé meta-sedimentary series with Mesoproterozoic-Early Neoproterozoic Nd model ages were derived from a protolith characterized by a mixture of juvenile Neoproterozoic and Paleoproterozoic sources without Archean contribution from the present adjacent Congo craton (Penaye et al., 1993; Toteu et al., 1994, 2001). This indicates the development of the Yaoundé series/basin in the internal zone of the Pan-African belt before being thrust onto the Congo craton (Toteu et al.,

2004). On the other hand, a significant amount of juvenile Neoproterozoic crustal component was recorded in the Neoproterozoic volcano-sedimentary schists and gneisses as well as Pan African granitoids from the Poli area, which is located to the northwest of the Central Cameroon-Tcholliré-Banyo shear zones in the Western Cameroon Domain (Toteu et al., 2004). This region may contain a small amount of 2.1 Ga crustal inheritance, but no Archean inheritance has been recognized (Toteu et al., 2001). The series of accretionary and collisional events from the Paleoproterozoic (Eburnian) to late Neoproterozoic in the Central African Fold Belt of Cameroon and other areas resulted in massive deformation/foliation phases expressed as several major shear zones/faulds (e.g., Tcholliré-Banyo, Central Cameroon, Southwest Cameroon, and Sanaga shear zones; Fig. 1b).

Accompanying the breakup of the Pangea, the opening of the South Atlantic Ocean began, along with rifting and formation of the Benue Trough in Nigeria since Early Cretaceous times. Since the Cenozoic, a 1600-km-long chain of volcanic complexes has existed, straddling the ocean-continent boundary from the Gulf of Guinea to the interior of the African plate as far as Lake Chad. This chain is known as the Cameroon Volcanic Line (CVL). The CVL is generally divided into three portions: the oceanic sector (including Annobon, Principe and São Tomé islands), the oceanic-continental boundary (including Bioko and Mt. Cameroon volcanoes) and the continental sector (including Manengouba, Bamboutou, Oku, Ngaoundéré Plateau and Biu Plateau). These volcanic rocks are dominated by alkali nephelinite/basanite/basalt, with more evolved rocks such as rhyolite and trachyte in the continental sector (Fitton, 1987). The similarity of chemical and isotopic signatures in basalts from both the oceanic and continental sectors indicates that the dominant mantle source resided in the asthenosphere instead of the lithospheric mantle (Déruelle et al., 2007; Assah et al., 2015, and reference therein). However, the absence of systematic geographic migration of volcanic activities over time in the CVL argues against a plume origin (Déruelle et al., 2007). The more evolved rocks reflect the fractional crystallization and/or crustal contamination. In summary, the CVL is regarded as a hotline along the previously formed lithospheric faults/shear zones tapping sub-lithospheric mantle (Meyers et al., 1998; Déruelle et al., 2007; Assah et al., 2015). Some CVL lavas erupted fragments of the lithospheric mantle that provides a precious opportunity to examine the nature of the lithospheric mantle and also to evaluate its role in the complex tectonic framework.

Mantle peridotite xenoliths chosen for this study were collected from Lake Nyos in the Oku volcanic field (Fig. 1). The major volcanic activity in the Nyos area occurred in the Quaternary (1.1–3.5 Ma determined by K-Ar dating of basalts; Freeth and Rex, 2000). The Precambrian basement of this area belongs to the Western Cameroon Domain, but resides <80 km away from the Central Cameroon shear zone (Fig. 1b). The eight peridotite xenoliths studied here are all fresh spinel lherzolites ranging from 6 cm to 15 cm in maximum dimension. Similar to the samples examined in previous studies on

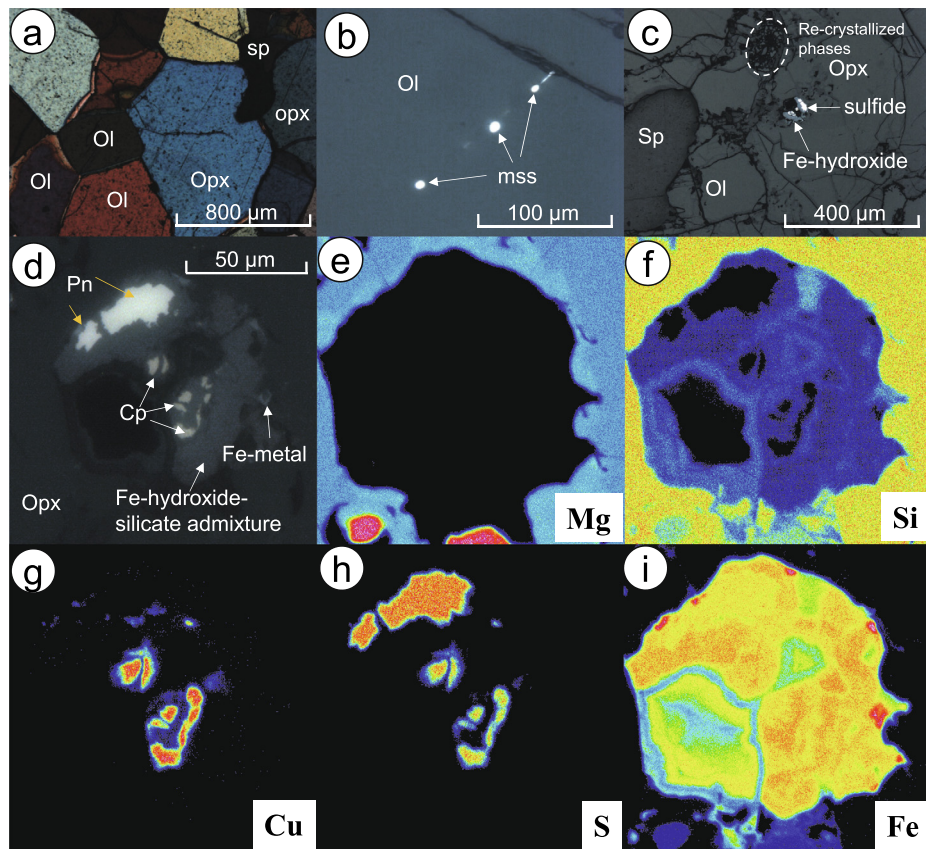


Fig. 2. (a–d) Photomicrographs of representative textures of the Nyos peridotites with an emphasis on the sulfide petrology. (e–i) X-ray elemental mapping of typical complex mineral assemblages associated with desulfurization. Abbreviation: Ol – olivine; Opx – orthopyroxene; Cpx – clinopyroxene; Sp – spinel.

the peridotites from Lake Nyos (Temdjim, 2012; Pintér et al., 2015; Liu et al., 2017), the samples in our study typically show protogranular to porphyroclastic texture (Fig. 2a) accompanied by clinopyroxene exsolution lamellae in orthopyroxene neoblasts and orthopyroxene/spinel lamellae in clinopyroxene grains, while no amphibole grains were found in our collection. The petrology and mineralogy of the xenoliths from this locality has been well described in these prior studies (Temdjim, 2012; Pintér et al., 2015; Liu et al., 2017). Here we place an emphasis on the sulfide petrology, as sulfides are major hosts to the HSE determined in this study and the state and abundance of sulfides will influence the Re-Os isotopic system in dating melt depletion of peridotites. We find that our Nyos peridotites are extremely poor in sulfides, with only a few sizable sulfides found in thin sections. The scarce sulfides have two typical forms. One is characterized by tiny ($<10 \mu\text{m}$) iron and nickel monosulfide solid solutions (Mss, $\text{Fe}_{(1-x)}\text{S-Ni}_{(1-x)}\text{S}$) that often form trails within the olivine or orthopyroxene grains (Fig. 2b). The other form is represented by larger complex mineral assemblages ($\sim 50\text{--}200 \mu\text{m}$) that appear within the olivine or orthopyroxene grains but close to the grain boundaries (Fig. 2c–d). These assemblages are rounded and consist in polymimetic blebs of pentlandite and chalcopyrite together with oxy-hydroxides (Fe-rich phases; Fig. 2e–i).

3. ANALYTICAL METHODS

Detailed analytical procedures used to produce the data in this study, as well as analytical precision and accuracy, are provided in the Electronic Annex EA-1. Here we briefly summarize the methods: (1) Major element compositions of peridotitic minerals on polished epoxy mounts or thin sections and sulfide mapping were determined/conducted using a JEOL 8900R Electron Probe Microanalyzer (EPMA) at the University of Alberta; (2) Trace element data for clinopyroxene and orthopyroxene were obtained on polished epoxy mounts using *in situ* laser ablation coupled with inductively coupled plasma-mass spectrometry (LA-ICP-MS) at the University of Alberta (see details in Liu et al., 2018); (3) Whole-rock major and minor element compositions were determined by X-ray fluorescence (XRF) on fused glass disks made from whole-rock powders (see Boyd and Mertzman (1987) for detailed protocols) at the Franklin and Marshall College, United States; (4) Whole-rock sulfur contents were determined at Macquarie University using an elemental analyzer from Elementar (EL-cube) fitted with an infrared detector for low S-content material; (5) Rhenium-Os isotopic compositions and HSE concentrations were determined using an isotope dilution technique coupled with High Pressure Asher (HPA-S, Anton Paar) digestion at the University of

Alberta, following the protocols of [Liu and Pearson \(2014\)](#) and [Harris et al. \(2018\)](#) and reference therein; and (6) The Sr-Nd-Hf isotope analyses for clinopyroxene and orthopyroxene were measured using isotope dilution at the University of Alberta, following the protocols of [Shu et al. \(2013\)](#).

4. RESULTS

Whole-rock major and minor element compositions as well as loss-on-ignition values of the Nyos peridotites are shown in [Table 1](#), and mineral major and trace element concentrations are provided in [Table 2](#) and [Table 3](#), respectively. These Nyos peridotites have moderate to high whole-rock Al_2O_3 (2.0–3.7%) and CaO (1.9–3.1%, sample CAM-022 up to 4.3%) contents ([Fig. 3a](#)), and low to moderate forsterite contents ($\text{Fo} = \text{molar Mg}/(\text{Mg} + \text{Fe}) \times 100 = 88.9\text{--}91.2$) of olivine and low Cr# (molar $\text{Cr}/(\text{Cr} + \text{Al}) \times 100 = 8.4\text{--}19.3$) of spinel. These peridotites have extremely low bulk sulfur contents ranging from 5.8 to 15.2 ppm except for CAM-022 that has a slightly higher S content of 28.7 ppm ([Table 1](#); [Fig. 3b](#)). The rare earth element (REE) patterns and trace element spider diagrams of both clinopyroxene and orthopyroxene are plotted in [Fig. 4a,b](#), respectively. Clinopyroxene generally exhibits limited to moderate depletions of LREE and nearly flat MREE to HREE, coupled with progressive depletions from HREE to LREE in orthopyroxene. The exception is sample

CAM 111, from which clinopyroxene and orthopyroxene both record progressive depletions of HREE to MREE with substantial enrichment of LREE. Systematic comparison of clinopyroxene and orthopyroxene shows that orthopyroxene can retain a significant amount of HREE and high strength field elements (Ti, Zr, Hf, Nb, Ta, U and Th) as a complementary host of these elements to clinopyroxene (e.g., [Rampone et al., 1991](#); [McDonough et al., 1992](#)). Moreover, the elemental ratios of orthopyroxene/clinopyroxene decrease from Lu to Sm, forming a linear trend with ionic radius except for some fluctuations from Nd to La ([Fig. 4c](#)).

We calculated equilibrium temperatures for the Nyos peridotites in two ways: (i) the two pyroxene REE thermometer of [Liang et al. \(2012\)](#) & (ii) the two pyroxene thermometer of [Brey and Köhler \(1990\)](#) based on major elements (assuming an equilibration pressure of 1.5 GPa for the latter approach). Both approaches yield overall consistent results with T_{REE} of 926–1043 °C and T_{BKN} of 942–1065 °C ([Table 1](#)), consistent with the range of equilibrium temperatures for the Nyos peridotites reported by [Liu et al. \(2017\)](#).

Whole-rock Re-Os isotopic compositions and HSE concentrations of the Nyos peridotites are shown in [Table 4](#). The primitive upper mantle (PUM)-normalized HSE patterns are plotted in [Fig. 5](#). These rocks display remarkable inter-element variations of HSE concentrations. For

Table 1

Major (oxides wt.%) and minor (ppm) element compositions of the Nyos peridotites as well as mineral modal abundances calculated by MINSQ and equilibrium temperatures.

Samples	CAM-020	CAM-022	CAM-101	CAM-102b	CAM-108	CAM-108b	CAM-109	CAM-111
SiO_2	43.72	43.47	43.52	44.15	43.32	43.64	43.86	43.80
TiO_2	0.18	0.12	0.14	0.08	0.11	0.10	0.12	0.01
Al_2O_3	3.59	3.42	3.44	2.44	3.60	2.74	3.71	2.01
$\text{Fe}_2\text{O}_3\text{T}$	9.37	9.79	9.53	8.28	9.04	9.26	8.43	8.44
MnO	0.13	0.13	0.13	0.11	0.12	0.12	0.12	0.11
MgO	38.76	37.38	39.22	41.79	39.65	40.49	39.61	42.56
CaO	2.87	4.32	2.90	2.02	3.07	2.53	3.05	1.90
Na_2O	0.27	0.27	0.23	0.20	0.26	0.23	0.29	0.10
K_2O	0.056	0.007	0.001	0.001	0.010	0.012	0.002	0.002
P_2O_5	0.026	0.043	0.012	0.014	0.014	0.017	0.012	0.006
Total	98.97	98.95	99.12	99.08	99.17	99.14	99.20	98.94
LOI	0.02	0.54	-0.13	0	-0.16	-0.13	-0.20	-0.11
Sr	25	36	6	7	6.5	15.5	10	1
Zr	16	5	10	4	3.5	6.5	11	5
V	68	73	73	48	68.5	53.0	66	48
Ni	2495	2742	2267	2568	2641	2686	1972	2699
Cr	2487	2912	2120	3078	3051	2193	2401	2818
Co	98	98	94	94	87.50	92.50	104	116
$S \pm 1\text{SD}$	8.3 ± 2.1	28.9 ± 6.8	9.7 ± 7.2	7.7 ± 2.3	11.7 ± 2.4	15.6 ± 4.6	8.9 ± 4.7	5.9 ± 3.2
Modal abundance (%)								
Olivine	59.0	61.2	62.9	66.5	64.0	66.4	62.4	69.4
Orthopyroxene	22.6	14.4	19.4	21.6	17.6	18.7	19.5	20.2
Clinopyroxene	14.0	20.4	14.1	9.4	14.4	11.9	14.6	8.0
Spinel	3.3	3.1	2.7	2.1	3.5	2.3	3.4	1.9
$T_{\text{REE}} (\text{°C} \pm 2\sigma)$	955 ± 18	926 ± 10	1043 ± 74	939 ± 30	969 ± 12	978 ± 22	968 ± 24	1028 ± 76
$T_{\text{BKN}} (\text{°C})$	1048	942	1065	1017	993	1009	990	976

Note: Mineral modal abundances are estimated using the MINSQ program ([Herrmann and Berry, 2002](#)); T_{REE} is calculated using the approach of [Liang et al. \(2012\)](#); T_{BKN} is calculated at $P = 1.5$ GPa using the equation of [Brey and Köhler \(1990\)](#)

Table 2

Mineral major element compositions (wt.%) of the Nyos peridotites determined by Electron Microprobe Analyzer.

Samples	SiO ₂	TiO ₂	Al ₂ O ₃	Cr ₂ O ₃	MnO	FeO	NiO	MgO	CaO	Na ₂ O	Total	n	Mg#
Olivine													
CAM-020	40.44		0.01		0.13	9.65	0.40	48.60	0.03		99.28	4	90.0
CAM-022	40.46		0.03		0.14	10.58	0.40	47.73	0.08		99.45	6	88.9
CAM-101	40.63		0.03		0.15	9.89	0.38	48.37	0.10		99.58	4	89.7
CAM-102b	40.79		0.02		0.12	8.49	0.38	49.28	0.07		99.19	4	91.2
CAM-108	40.58		0.02		0.14	9.57	0.38	48.48	0.07		99.30	8	90.0
CAM-108b	40.71		0.03		0.14	9.57	0.38	48.46	0.07		99.41	6	90.0
CAM-109	40.72		0.01		0.13	9.26	0.37	48.58	0.06		99.17	5	90.3
CAM-111	40.72		0.03		0.13	8.50	0.39	49.26	0.09		99.14	5	91.2
<i>San Carlos</i>	41.16		0.01		0.12	8.93	0.38	49.57	0.07		100.3	4	90.8
Orthopyroxene													
CAM-020	55.37	0.09	3.89	0.3	0.15	6.16	0.09	32.76	0.45	0.07	99.33	5	90.5
CAM-022	55.52	0.07	3.49	0.28	0.15	6.71	0.10	32.59	0.49	0.09	99.49	5	89.7
CAM-101	54.95	0.13	4.55	0.28	0.14	6.27	0.10	32.21	0.62	0.11	99.38	5	90.2
CAM-102b	55.70	0.10	3.63	0.42	0.12	5.41	0.09	33.28	0.55	0.11	99.42	5	91.6
CAM-108	55.35	0.10	3.97	0.30	0.14	6.06	0.09	32.59	0.58	0.10	99.26	6	90.6
CAM-108b	55.38	0.10	3.97	0.31	0.14	6.04	0.09	32.66	0.58	0.10	99.40	7	90.6
CAM-109	55.33	0.10	4.01	0.31	0.14	5.91	0.09	32.82	0.56	0.11	99.38	5	90.8
CAM-111	55.71	0.04	3.45	0.4	0.12	5.40	0.11	33.25	0.60	0.07	99.18	5	91.7
Clinopyroxene													
CAM-020	52.33	0.42	6.43	0.75	0.08	2.60	0.05	15.55	19.62	1.64	99.51	6	91.4
CAM-022	52.30	0.45	6.08	0.79	0.07	2.78	0.04	14.70	20.56	1.59	99.39	6	90.4
CAM-101	51.95	0.59	6.97	0.62	0.09	2.94	0.05	15.13	19.31	1.69	99.39	7	90.2
CAM-102b	52.81	0.48	6.04	1.11	0.06	2.35	0.05	15.17	19.75	1.86	99.71	7	92.0
CAM-108	52.50	0.49	6.18	0.75	0.08	2.54	0.05	15.15	20.25	1.61	99.64	8	91.4
CAM-108b	52.48	0.49	6.16	0.76	0.08	2.59	0.04	15.20	19.99	1.67	99.50	7	91.3
CAM-109	52.60	0.49	6.51	0.75	0.08	2.49	0.04	14.87	19.93	1.86	99.62	6	91.4
CAM-111	53.02	0.12	4.44	0.88	0.07	2.27	0.05	16.34	21.40	1.01	99.63	8	92.8
<i>DUR</i>	55.51	0.13	0.26	0.36	0.06	1.55	0.03	17.93	24.56	0.34	100.7	11	95.4
Spinel													
CAM-020	0.07	0.07	57.82	9.85	0.10	10.63	0.38	20.54			99.61	4	10.3
CAM-022	0.07	0.1	56.22	10.80	0.09	11.89	0.39	20.08			99.77	5	11.4
CAM-101	0.09	0.18	58.99	8.06	0.09	10.50	0.39	21.08			99.52	6	8.4
CAM-102b	0.07	0.13	51.82	16.42	0.09	10.45	0.32	20.42			99.85	6	17.5
CAM-108	0.09	0.12	56.86	10.70	0.09	10.53	0.37	20.68			99.57	6	11.2
CAM-108b	0.08	0.12	56.88	10.61	0.09	10.59	0.38	20.78			99.64	6	11.1
CAM-109	0.09	0.12	57.41	10.07	0.08	10.35	0.38	20.92			99.51	6	10.5
CAM-111	0.09	0.05	50.19	17.93	0.09	10.76	0.34	20.22			99.80	11	19.3
<i>EPS1</i>	0.08	0.11	10.44	60.19	0.13	12.88	0.17	16.66			100.7	7	79.5

Note: blank means below detection limit (<0.01%); San Carlos olivine, Dur Cr-diopside and EPS1 spinel are used as unknowns. Mg# = molar ($Mg/(Mg + Fe)$) × 100, Cr# = molar Cr/(Cr + Al) × 100. Uncertainties are provided in the Electronic Annex EA-2 (Table S1).

instance, their Ir (2.72–4.49 ppb) and Ru (5.63–9.76 ppb) concentrations lie in the range of primitive upper mantle (PUM; Becker et al., 2006), while their Os (0.83–2.58 ppb), Pd (1.42–5.28 ppb) ppb, and Re (0.021–0.067 ppb) concentrations are significantly lower than those of PUM estimates; the Pt concentrations range from 3.26 to 8.56 ppb, which are lower than or comparable to that of PUM. As a result, these peridotites exhibit low chondrite-normalized Os_N/Ir_N (0.28–0.63), Pd_N/Ir_N (0.39–1.55) and Re_N/Ir_N (0.07–0.26) ratios (Fig. 6), and are characterized by convex, arc shape-like fractionated HSE patterns (Fig. 5). The Nyos peridotites have ¹⁸⁷Os/¹⁸⁸Os ratios ranging from 0.1198 to 0.1282 yielding T_{RD} and T_{MA} ages of 0–1.2 Ga and 0–1.4 Ga, respectively. A Re-Os isochron diagram and the correlation between Al₂O₃ and ¹⁸⁷Os/¹⁸⁸Os are presented in Fig. 7a&b, respectively.

Strontium, Nd and Hf isotopic data of both clinopyroxene and orthopyroxene of the selected five Nyos peridotites are provided in Table 5. The Nyos clinopyroxene has a narrow range of ⁸⁷Sr/⁸⁶Sr (0.70210–0.70296) that is lower than that of the host basalt (0.70356), while the orthopyroxene did not have enough Sr to produce high-quality isotopic data. There are some differences in the concentrations of Sm, Nd, Lu and Hf determined between using the laser ablation (LA) and isotope dilution (ID) methods. For clinopyroxene, the ID concentrations of these elements are generally slightly higher than the LA data (Nd 4.8–8.7%, Sm 16.6–27%, Lu 3.4–17.7%, and Hf 6.6–33%; Table 5). For orthopyroxene, the ID Sm and Nd concentrations are generally lower than, or similar to, the LA counterparts (Nd –38–10%, Sm –35–19.6%) primarily due to extremely low concentrations that could have led to large

Table 3

Mineral elemental concentrations (ppm) of clinopyroxene and orthopyroxene from the Cameroon peridotites determined using in situ laser ablation ICP-MS.

Samples	Clinopyroxene								Orthopyroxene							
	CAM-020	CAM-022	CAM-101	CAM-102b	CAM-108	CAM-108b	CAM-109	CAM-111	CAM-020	CAM-022	CAM-101	CAM-102b	CAM-108	CAM-108b	CAM-109	CAM-111
Sc	66.0	65.2	65.7	73.2	69.3	69.0	68.6	71.7	15	12	16	14	15	14	14	18
Ti	2896	2936	4053	3190	3220	3173	3217	772	525	473	814	623	655	643	640	216
V	283	283	308	325	296	293	313	272	88	75	95	85	91	89	90	90
Cr	5508	5775	4645	8072	5605	5628	5745	6895	2094	1839	1884	2802	2244	2195	2132	2820
Mn	685	734	831	618	754	742	740	679	1165	1212	1116	971	1156	1137	1107	1024
Co	18.5	22.9	25.4	22.1	21.2	21.3	20.7	21.5	57.5	65.0	64.3	58.3	62.4	62.8	61.0	61.9
Ni	315	362	416	362	376	366	367	425	751	809	872	818	824	853	822	913
Cu	1.45	1.16	0.90	1.36	1.23	1.17	1.14	0.82	0.85	1.18	0.74	0.98	1.14	1.15	1.13	1.00
Zn	6.55	8.96	10.97	8.49	7.45	7.66	7.46	8.20	28.3	34.9	38.5	33.9	33.1	32.8	31.3	35.3
Ga	3.19	3.25	3.98	3.19	3.08	3.08	3.38	1.91	2.45	2.70	3.39	2.55	2.58	2.60	2.76	1.87
Rb	0.024	0.010	0.007	0.014	0.012	0.007	0.011	0.008	0.0036	0.0025	0.0032	0.0030	0.023	0.017	0.022	0.0085
Sr	30.7	75.2	46.8	61.8	51.2	52.2	74.6	13.1	0.094	0.098	0.081	0.082	0.083	0.060	0.127	0.023
Y	16.9	14.8	18.5	15.5	16.8	16.4	17.1	7.5	0.752	0.66	1.23	0.80	0.90	0.90	0.88	0.53
Zr	18.8	25.8	22.5	27.1	24.0	24.6	26.4	6.3	0.766	0.77	1.17	0.92	0.98	0.97	1.19	0.44
Nb	0.08	0.16	0.26	0.05	0.08	0.27	0.03	0.18	0.0034	0.0039	0.0045	0.0028	0.0051	0.0038	0.0035	0.0107
Sn	0.17	0.21	0.29	0.29	0.26	0.29	0.29	0.04	0.026	0.019	0.029	0.031	0.0233	0.0287	0.0304	0.0065
Ba	0.62	0.03	0.03	0.05	0.03	0.02	0.07	0.02	0.038	0.0026	0.0060	0.0031	0.0026	0.0036	0.0066	0.0029
La	0.20	2.17	0.55	0.88	0.51	1.14	0.80	0.70	0.0020	0.0028	0.0025	0.0017	0.0023	0.0013	0.0022	0.0020
Ce	1.00	3.95	2.76	3.18	2.20	2.96	3.42	0.86	0.023	0.0138	0.021	0.018	0.0148	0.0077	0.0172	0.0072
Pr	0.25	0.55	0.55	0.61	0.45	0.54	0.72	0.09	0.0013	0.0018	0.0031	0.0017	0.0017	0.0016	0.0028	0.0005
Nd	2.01	3.20	3.74	3.82	3.10	3.25	4.74	0.48	0.011	0.0094	0.020	0.012	0.012	0.013	0.019	0.0032
Sm	1.16	1.38	1.68	1.56	1.42	1.39	1.84	0.27	0.0089	0.0084	0.013	0.0123	0.0099	0.0107	0.0163	0.0022
Eu	0.53	0.58	0.71	0.63	0.60	0.58	0.73	0.14	0.0057	0.0051	0.0099	0.0052	0.0073	0.0065	0.0082	0.0025
Gd	2.04	1.99	2.57	2.21	2.19	2.13	2.43	0.64	0.028	0.025	0.053	0.031	0.033	0.038	0.037	0.013
Tb	0.39	0.37	0.46	0.39	0.40	0.39	0.42	0.13	0.0083	0.0072	0.015	0.0088	0.010	0.011	0.010	0.0050
Dy	2.92	2.62	3.31	2.86	2.93	2.92	3.03	1.15	0.084	0.072	0.144	0.094	0.104	0.107	0.108	0.056
Ho	0.65	0.57	0.70	0.58	0.63	0.62	0.64	0.28	0.026	0.023	0.042	0.026	0.031	0.030	0.030	0.018
Er	1.97	1.69	2.11	1.75	1.92	1.87	1.93	0.92	0.114	0.097	0.168	0.111	0.134	0.130	0.133	0.085
Tm	0.28	0.24	0.30	0.24	0.27	0.27	0.28	0.14	0.026	0.020	0.035	0.024	0.028	0.026	0.028	0.017
Yb	1.87	1.61	2.01	1.55	1.82	1.76	1.86	0.95	0.207	0.179	0.272	0.176	0.225	0.214	0.230	0.156
Lu	0.26	0.22	0.27	0.20	0.25	0.24	0.26	0.14	0.039	0.032	0.050	0.032	0.040	0.039	0.040	0.026
Hf	0.72	0.81	0.93	0.76	0.83	0.81	0.97	0.11	0.031	0.027	0.040	0.021	0.033	0.031	0.036	0.0066
Ta	0.00	0.03	0.01	0.01	0.01	0.01	0.01	0.02	0.0008	0.0003	0.0003	0.0002	0.0003	0.0002	0.0007	0.0005
Pb	0.05	0.20	0.04	0.62	0.11	0.17	0.23	0.08	0.0042	0.0047	0.0052	0.0057	0.0065	0.0051	0.0059	
Th	0.01	0.68	0.06	0.15	0.04	0.22	0.01	0.23	0.0026	0.0060	0.0006	0.0015	0.0007	0.0005	0.0007	0.0019
U	0.01	0.12	0.01	0.11	0.02	0.08	0.01	0.07	0.0009	0.0023	0.0009	0.0035	0.0006	0.0009	0.0014	0.0018
n	6	6	8	8	8	6	6	5	5	5	5	6	6	5	5	

Uncertainties are provided in the Electronic Annex 2 (Table S2).

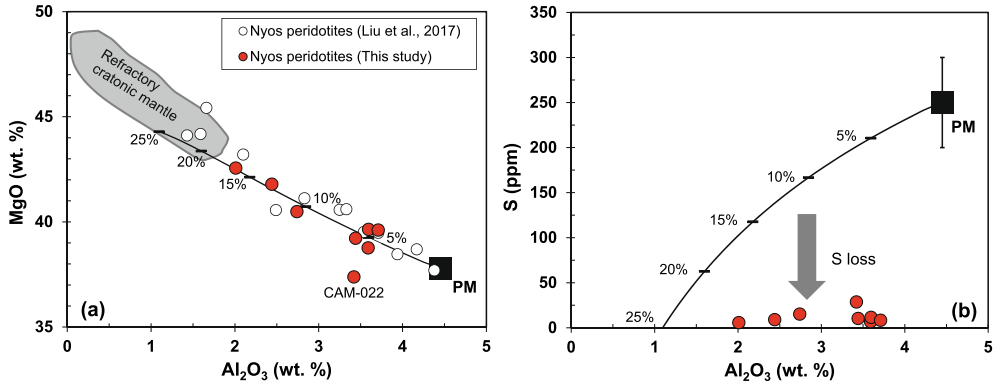


Fig. 3. Whole-rock Al₂O₃ vs. MgO (a) and S (b) of peridotites from Lake Nyos, Mt. Oku. Melting curve for major elements from a primitive mantle source (PM: McDonough and Sun, 1995) follows that of Niu (1997), and for S content assuming that the extracted melts have a S capacity of 1000 ppm (Jugo et al., 2005). Gray field shows typical cratonic mantle composition (Pearson and Wittig, 2008, and references therein). Also shown are the data of Nyos peridotites from Liu et al. (2017).

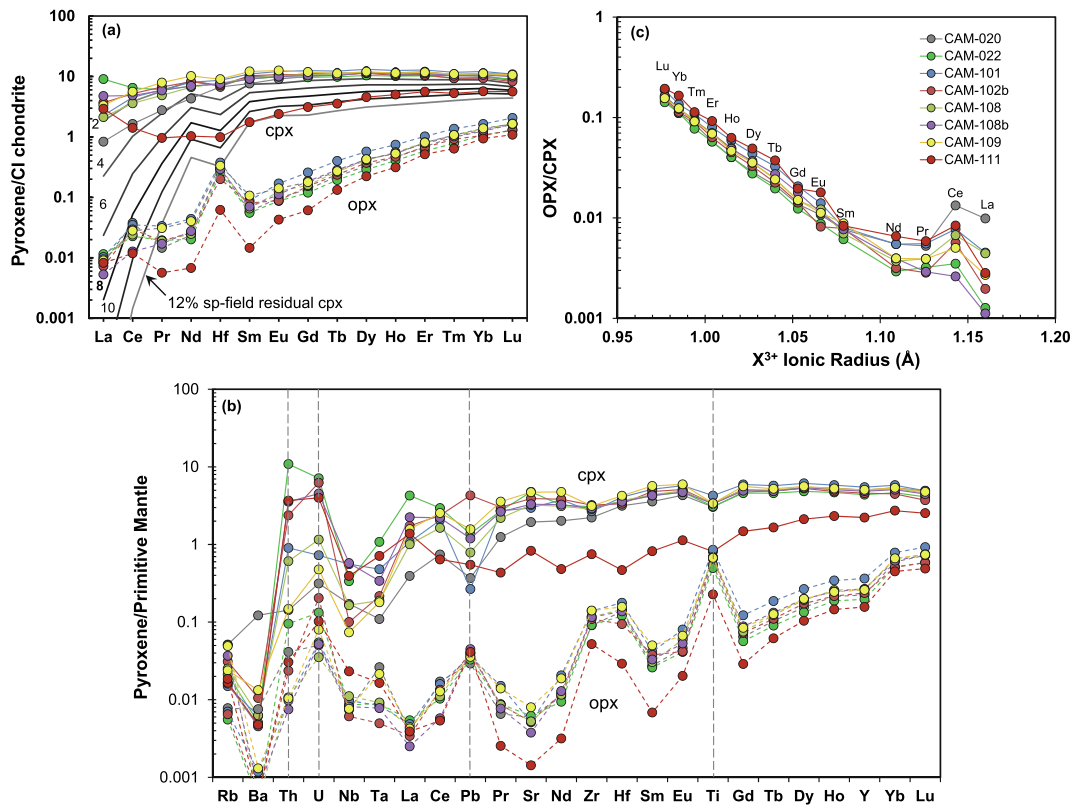


Fig. 4. Chondrite-normalized REE patterns (a) and primitive mantle-normalized trace element spider diagram (b) of both clinopyroxene (symbols with solid lines) and orthopyroxene (symbols with dashed lines) from the Nyos peridotites examined in this study. The REE elemental ratios of orthopyroxene/clinopyroxene are plotted as a function of ionic radius in (c). Chondrite composition: Sun and McDonough (1989); Primitive mantle composition: McDonough and Sun (1995). Grey lines are the modeled results for residual clinopyroxene assuming non-modal fractional melting in the spinel stability field (see the details in Liu et al. (2012) and reference therein). Literature data are shown in Fig. S5.

bias for the LA data, while the ID Lu and Hf concentrations are largely higher than the LA data (Lu 8.6–15.4%, Hf –4.3–39%). Despite having considerably higher Sm/Nd ratios than its coexisting clinopyroxene, orthopyroxene within CAM-102b and CAM-109 has ¹⁴³Nd/¹⁴⁴Nd only slightly greater than that of coexisting clinopyroxene, giving

positive two-point clinopyroxene-orthopyroxene Sm-Nd isochron ages (Table 5), while the other three samples (CAM-020, CAM-108 and CAM-111) have clinopyroxene ¹⁴³Nd/¹⁴⁴Nd identical to, or slightly greater than, that of the coexisting orthopyroxene, yielding near zero or slightly negative two-point isochron ages (Table 5). The Nd model

Table 4
Highly siderophile element concentrations (ppb) and Re-Os isotopic compositions of the Nyos peridotites.

Sample	Os	2σ	Ir	2σ	Ru	2σ	Pt	2σ	Pd	2σ	Re	2σ	$^{187}\text{Re}/^{188}\text{Os}$	2σ	$^{187}\text{Os}/^{188}\text{Os}$	2σ	$^{187}\text{Re}/^{188}\text{Os}$	2σ	$^{187}\text{Os}/^{188}\text{Os}$	2σ	T_{RD}	T_{MA}
CAM-020	0.827	0.010	2.93	0.06	5.69	0.09	3.25	0.07	1.42	0.04	0.030	0.001	0.175	0.004	0.12550	0.00010	0.40	0.68				
CAM-022	2.329	0.016	3.68	0.13	7.89	0.13	6.35	0.21	4.34	0.13	0.061	0.001	0.127	0.002	0.12453	0.00009	0.53	0.76				
CAM-101	1.252	0.012	2.91	0.04	5.91	0.08	5.36	0.10	2.60	0.05	0.052	0.001	0.200	0.003	0.12798	0.00009	0.05	0.09				
CAM-102b	1.473	0.012	3.56	0.11	7.45	0.09	3.81	0.09	2.70	0.08	0.021	0.001	0.069	0.001	0.11984	0.00008	1.19	1.42				
CAM-108	1.840	0.014	2.93	0.12	6.63	0.08	5.49	0.21	4.38	0.12	0.048	0.001	0.126	0.003	0.12513	0.00009	0.45	0.64				
CAM-108b	2.266	0.016	3.60	0.43	7.94	0.21	5.65	0.56	4.67	0.22	0.067	0.004	0.142	0.008	0.12493	0.00009	0.48	0.72				
CAM-109	1.716	0.013	2.72	0.09	5.63	0.10	4.73	0.17	5.20	0.23	0.060	0.001	0.169	0.004	0.12818	0.00009	0.02	0.03				
CAM-111	2.583	0.017	4.49	0.16	9.76	0.15	8.56	0.31	5.28	0.13	0.058	0.001	0.056	0.001	0.12067	0.00009	1.08	1.24				

Note: Uncertainties (2σ) are calculated by thorough error propagation. Os model ages are calculated using the ordinary chondritic mantle reference ($^{187}\text{Re}/^{188}\text{Os} = 0.422$, $^{187}\text{Os}/^{188}\text{Os} = 0.1283$; Horan et al., 2003; $\lambda = 1.666 \times 10^{-11} \text{ yr}^{-1}$).

ages of the clinopyroxene in most samples are generally older than those of the orthopyroxene ($T_{\text{DM}}(\text{Nd}) = 0.25\text{--}0.90 \text{ Ga}$ versus $0.17\text{--}0.40 \text{ Ga}$, and $T_{\text{CHUR}}(\text{Nd}) = 1.01\text{--}1.17 \text{ Ga}$ versus $0.45\text{--}0.74 \text{ Ga}$), except for the most fertile sample CAM-109 that has much lower or negative values ($T_{\text{DM}}(\text{Nd}) = -0.80 \text{ Ga}$ versus -0.22 Ga , and $T_{\text{CHUR}}(\text{Nd}) = 0.25 \text{ Ga}$ versus 0.33 Ga) and has a significantly positive two-point isochron age (Table 5).

Unlike the Sm-Nd isotope system, orthopyroxene has Lu/Hf ratios three to five times of those of clinopyroxene, and the orthopyroxene $^{176}\text{Hf}/^{177}\text{Hf}$ ratios are identical to, or significantly larger than, those of coexisting clinopyroxene. Both clinopyroxene and orthopyroxene generally have higher $^{143}\text{Nd}/^{144}\text{Nd}$ and $^{176}\text{Hf}/^{177}\text{Hf}$ ratios than the host lavas, except for the most fertile sample CAM-109 that has $^{143}\text{Nd}/^{144}\text{Nd}$ slightly lower in clinopyroxene but slightly higher in orthopyroxene than the host lava. Because the majority of Sm and Nd (>98%) in these samples are hosted in clinopyroxene, the limited variation of $^{143}\text{Nd}/^{144}\text{Nd}$ in both clinopyroxene and orthopyroxene means that the reconstructed whole-rock Sm/Nd and $^{143}\text{Nd}/^{144}\text{Nd}$ for each sample are essentially identical to the values in clinopyroxene. The reconstructed whole-rock Sm-Nd isochron yields an apparent age of $1.37 \pm 0.39 \text{ Ga}$ (1σ ; MSWD = 51; an initial ε_{Nd} of -8 ± 8 (1σ); Fig. 8a), and the reconstructed whole-rock Lu-Hf isochron gives an age of $2.01 \pm 0.18 \text{ Ga}$ (1σ ; MSWD = 11.4; Fig. 8b) with an initial ε_{Hf} of -0.8 ± 9.6 (1σ).

5. DISCUSSION

5.1. History of melt depletion and metasomatic overprinting

5.1.1. Melt depletion

Mantle melt extraction shapes the mineralogy and chemistry of residual peridotite, changing fertile lherzolite into depleted harzburgite. The mineral modal abundances of the Nyos peridotites examined in this study are calculated using the MINSQ program (Herrmann and Berry, 2002) through combination of both mineral and whole-rock major element data. The results show that these Nyos peridotites are composed of olivine (59–69%), orthopyroxene (14–23%), clinopyroxene (8–20%), and spinel (1.9–3.5%) (Table 1). All the Nyos peridotites are categorized as spinel facies lherzolites (Fig. S1; Electronic Annex EA-1), except for sample CAM-022 which has significantly higher clinopyroxene (20%) and lower orthopyroxene (14%). In addition to lherzolites, previous studies have reported harzburgites and olivine websterites from this locality (Fig. S1; Temdjem, 2012; Pintér et al., 2015; Liu et al., 2017).

Mineral and whole-rock chemistries are the key to estimate the degrees of apparent melt depletion of the Nyos peridotites, as auto-refertilization/metasomatism may have occurred in nearly all mantle peridotites (Rudnick and Walker, 2009; Fig. S2a). Our Nyos peridotites are characterized by low to moderate olivine Fo contents of 88.9–91.2 and low spinel Cr# of 8.4–19.3, plotting within the range found in prior studies (Fo = 89.8–92.0; spinel Cr# = 9.6–37.2; Fig. S3; Temdjem, 2012; Pintér et al.,

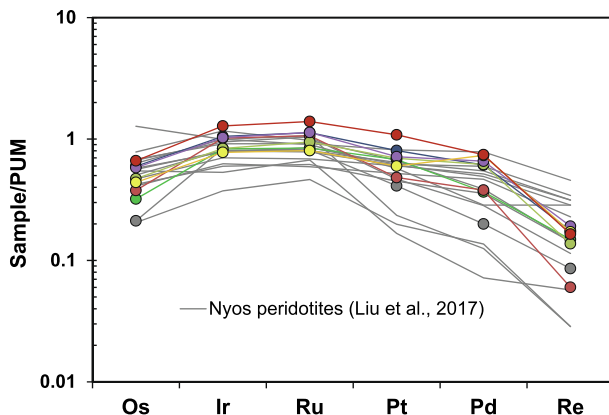


Fig. 5. Primitive Upper Mantle (PUM: Becker et al., 2006)-normalized highly siderophile element patterns of the Nyos peridotites. Also shown are the data of Nyos peridotites from Liu et al. (2017).

2015; Liu et al., 2017). Using an experimental curve of melting degree versus Fo contents of residual olivine (Bernstein et al., 2007), we found that the Nyos peridotites experienced variable degrees of partial melting ranging from a few percent to ~15–20% for lherzolites in this suite, and up to 25% for harzburgites in other Nyos peridotites (Liu et al., 2017). Moreover, the Nyos peridotites in our suite have moderate to high whole-rock Al_2O_3 (2.0–3.7%) and CaO (1.9–3.1%) contents, which plot within the melt depletion trend (Fig. 3a; Fig. S2b). The exception is sample CAM-022 with 4.3% CaO (plotting above PUM), due to modal metasomatic overprinting/refertilization as will be discussed below. For the rest of the Nyos peridotites in our suite, they can be explained by ~5–16% batch melting at 1.5 GPa following the model of Niu (1997), which is in concordance with the estimate from Fo contents discussed above, derived from an experimental calibration of batch melts. In addition, incompatible trace element abundances in

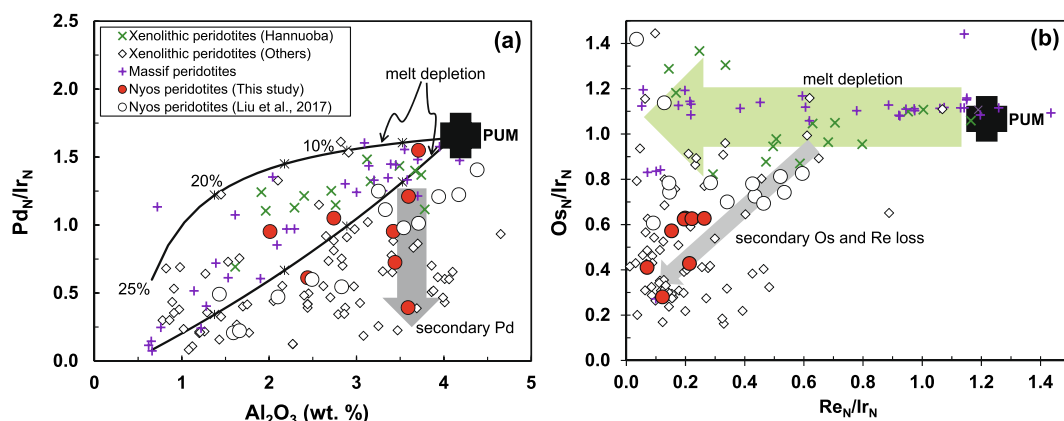


Fig. 6. (a) Whole-rock Pd_N/Ir_N versus Al_2O_3 and (b) Os_N/Ir_N versus Re_N/Ir_N for xenolithic peridotites from Nyos and other areas globally compared to massif peridotites. Melt extraction curves were calculated in the form of non-modal, fractional melting using a primitive mantle source containing ~250 ppm S (McDonough and Sun, 1995) and assuming that the extracted melts have a S capacity of 1000 ppm (Jugo et al., 2005). The partition coefficients between sulfide and silicate melt used in the two modeling curves are: D_{Pd} (sulfide/melt) of 10^4 and 10^3 for the upper curve and lower curve, respectively; and $D_{\text{I}}(\text{sulfide}/\text{melt})$ was set at 10^5 (Fleet et al., 1999). Tick marks indicate 5% melting increments. Data sources: Nyos peridotites from Liu et al., 2017 and this study; global xenolith data (including Vitim, Siberia; Hannuoba, Yangyuan, Penglai, Shanwang from China; Sierra Nevada, USA; Sidamo, Ethiopia; North Queensland, Australia) and massif data (including Pyrenees, France; Beni Bousera, Morocco; Ronda, Spain; Italian Alps; Lower Austria; Rhode Island, USA) are referred to the compilation of Liu et al. (2010) and references therein. PUM: Becker et al. (2006).

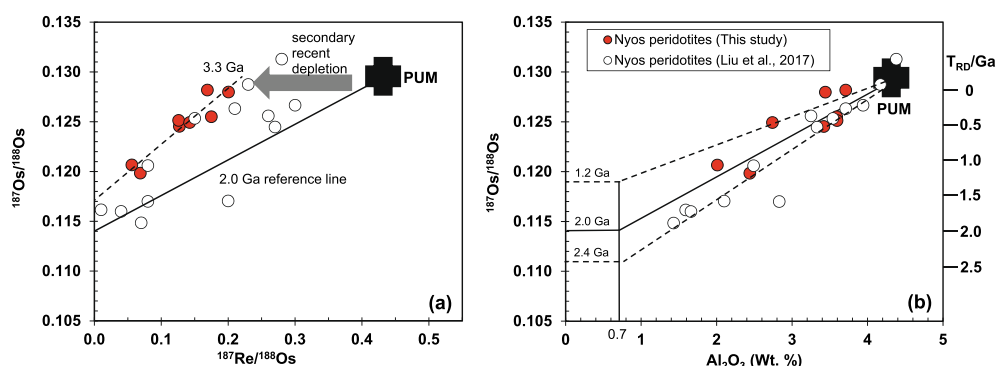


Fig. 7. (a) The Re-Os isochron diagram and (b) whole-rock $^{187}\text{Os}/^{188}\text{Os}$ versus Al_2O_3 for the Nyos peridotites (Liu et al., 2017; this study). PUM: Meisel et al. (2001).

Table 5

Sr, Nd and Hf isotopic compositions of clinopyroxene and orthopyroxene separates of the Nyos peridotites as well as the calculated whole-rock compositions and host basalt (CAM-108 basalt).

Sample	CAM-020	CAM-020	CAM-020	CAM-102b	CAM-102b	CAM-102b	CAM-108	CAM-108	CAM-109	CAM-109	CAM-109	CAM-111	CAM-111	CAM-111	BHVO-1	CAM-108 basalt	
	CPX	OPX	WR	CPX	OPX	WR	CPX	OPX	WR	CPX	OPX	WR	CPX	OPX	WR	WR	
Weight (g)	0.05972	0.28211		0.05241	0.32031		0.06658	0.30301		0.05744	0.32174		0.20903	0.52584		0.02099	0.05496
Rb [ppm]-LA	0.024	0.0036		0.014	0.0030		0.012	0.0231		0.011	0.0225		0.008	0.0085			
Sr [ppm]-LA	30.7	0.094		61.8	0.082		51.2	0.083		74.6	0.127		13.1	0.023			
$^{87}\text{Sr}/^{86}\text{Sr}$	0.702257			0.702417			0.702100			0.702864			0.702956			0.703450	0.703558
2σ	0.000016			0.000012			0.000011			0.000013			0.000019			0.000021	0.000022
Sm [ppm]-ID	1.393	0.00590	0.196	2.000	0.00799	0.190	1.784	0.00799	0.259	2.394	0.01166	0.351	0.365	0.00169	0.030	7.633	7.759
Sm [ppm]-LA	1.16	0.0089		1.56	0.0123		1.42	0.0099		1.84	0.0163		0.27	0.0022			
Nd [ppm]-ID	2.109	0.00682	0.297	4.183	0.01041	0.396	3.333	0.01228	0.483	5.135	0.02061	0.751	0.506	0.00219	0.041	24.96	37.87
Nd [ppm]-LA	2.01	0.0110		3.82	0.0121		3.10	0.0115		4.74	0.0187		0.48	0.0032			
$^{147}\text{Sm}/^{144}\text{Nd}$	0.3996	0.5235	0.4003	0.2891	0.4642	0.2901	0.3238	0.3933	0.3241	0.2818	0.3421	0.2821	0.4362	0.4659	0.4365	0.1849	0.1239
$^{143}\text{Nd}/^{144}\text{Nd}$	0.513980	0.513952	0.513980	0.513252	0.513412	0.513253	0.513611	0.513591	0.513611	0.512770	0.512943	0.512771	0.514452	0.513653	0.514443	0.512962	0.512834
2σ	0.000019	0.000157	0.000019	0.000013	0.000071	0.000013	0.000019	0.000074	0.000019	0.000017	0.000055	0.000017	0.000036	0.000112	0.000036	0.000010	0.000011
T _{DM} (Ga)	0.69	0.40	0.69	0.25	0.17	0.24	0.66	0.39	0.66	-0.80	-0.22	-0.79	0.90	0.32	0.90		
T _{CHUR} (Ga)	1.01	0.62	1.01	1.02	0.45	1.01	1.17	0.74	1.17	0.25	0.33	0.25	1.16	0.58	1.15		
Two-point isochron age (Ma)				-35 ± 190			140 ± 62			-44 ± 160			439 ± 150			-4170 ± 1900	
Lu [ppm]-ID	0.3083	0.0430	0.0529	0.2423	0.0351	0.0304	0.2916	0.0459	0.0501	0.3132	0.0469	0.0547	0.1417	0.0313	0.0177	0.2868	0.2434
Lu [ppm]-LA	0.26	0.0393		0.20	0.0315		0.25	0.0404		0.26	0.0400		0.14	0.0264			
Hf [ppm]-ID	0.7844	0.0298	0.1165	0.8241	0.0250	0.0829	0.8913	0.0341	0.1345	1.0685	0.0390	0.1631	0.1586	0.0108	0.0149	4.229	4.732
Hf [ppm]-LA	0.72	0.0310		0.76	0.0214		0.83	0.0330		0.97	0.0358		0.11	0.0066			
$^{176}\text{Lu}/^{177}\text{Hf}$	0.0558	0.2051	0.0643	0.0417	0.1994	0.0519	0.0464	0.1911	0.0528	0.0416	0.1710	0.0476	0.1269	0.4096	0.1682	0.0096	0.0073
$^{176}\text{Hf}/^{177}\text{Hf}$	0.283623	0.286545	0.283791	0.283645	0.283908	0.283662	0.283618	0.283479	0.283612	0.283137	0.283454	0.283152	0.287652	0.289558	0.287932	0.283088	0.282989
2σ	0.000017	0.000056	0.000017	0.000016	0.000021	0.000021	0.000022	0.000085	0.000022	0.000014	0.000031	0.000013	0.000064	0.0000274	0.000068	0.000015	0.000007
ϵHf	30.1	133.4	36.0	30.9	40.2	31.5	29.9	25.0	29.7	12.9	24.1	13.4	172.6	240.0	182.5	11.2	7.7
T _{DM} (Ga)	1.14	1.05	1.11	5.99	0.22	1.61	2.40	0.08	1.33	-1.92	0.08	-0.58	2.60	0.90	1.90	0.30	0.45
T _{CHUR} (Ga)	1.98	1.16	1.73	5.22	0.37	2.49	3.32	0.24	2.24	2.28	0.26	1.40	2.72	0.96	2.01	-0.72	-0.45
Two-point isochron age (Ma)				1039 ± 35			89 ± 73			-52 ± 32			131 ± 14			360 ± 53	

Abb reviation: LA - laser ablation data; ID - isotope dilution data; CPX - clinopyroxene; OPX - orthopyroxene; WR - Reconstructed Whole Rock data using CPX and OPX assuming olivine and spinel contain none of the elements considered.

Chondritic Uniform Reservoir (CHUR) values: $^{147}\text{Sm}/^{144}\text{Nd} = 0.1960$, $^{143}\text{Nd}/^{144}\text{Nd} = 0.512630$, $^{176}\text{Lu}/^{177}\text{Hf} = 0.0336$ and $^{176}\text{Hf}/^{177}\text{Hf} = 0.282785$ (Bouvier et al., 2008)

T_{DM}(Nd) is calculated based on the depleted mantle values ($^{147}\text{Sm}/^{144}\text{Nd} = 0.2129$ and $^{143}\text{Nd}/^{144}\text{Nd} = 0.51313$; Nowell et al., 1998; Bouvier et al., 2008)

T_{DM}(Hf) is calculated based on the depleted mantle values ($^{176}\text{Lu}/^{177}\text{Hf} = 0.0388$ and $^{176}\text{Hf}/^{177}\text{Hf} = 0.28325$; Nowell et al., 1998; Bouvier et al., 2008)

minerals can also be used to constrain melt depletion characteristics. We model the REE and Hf composition of residual clinopyroxene (the main carrier of these elements in spinel facies lherzolite) in the scenario of non-modal, fractional melting following the method of Johnson et al. (1990) (see details in Liu et al. (2012)). The modeling is conducted in the spinel stability field, as there is no garnet or observation of garnet breakdown in the Nyos peridotites. Based on the relatively immobile HREE, the Nyos peridotites are residues of a few percent up to ~12% fractional melt extraction (Fig. 4a; Fig. S4), somewhat lower than estimates from batch-melting calibrations. In reality, natural melting is likely somewhere between pure batch and pure fractional melting and so these estimates bracket the likely extent of actual melting. Collectively, the Nyos peridotites in our collection are mantle residues of variable degrees of melt depletion ranging from a few percent up to a maximum of ~16%. We find that some of the Nyos clinopyroxenes and orthopyroxenes, particularly the more depleted ones, have LREE contents too high to be pristine melt residues. This has been observed in the Nyos peridotites in prior studies and in global mantle peridotites, and has been ascribed to metasomatic alteration/enrichment.

5.1.2. Metasomatic overprinting

Metasomatism has almost ubiquitously affected mantle peridotite. This process can be divided into broad two types: modal versus cryptic metasomatism. As stated above, sample CAM-022 has extreme signatures of mineralogical and geochemical characteristics. This sample is a clinopyroxene-rich lherzolite that is characterized by the lowest abundance of orthopyroxene (14%) and the highest abundance of clinopyroxene (22%), but moderate modal abundance of olivine (61%) relative to other samples in the suite (Table 1). Moreover, CAM-022 has the highest bulk rock CaO content (4.32 wt.%, higher than that of primitive mantle; McDonough and Sun, 1995), intermediate Al₂O₃ content (3.42 wt.%), the highest CaO/Al₂O₃ ratio

(1.26, compared to the range of 0.83–0.95 for the main suite) and the lowest MgO/SiO₂ (0.86, compared to the range of 0.89–0.97 for the main suite). These features are coupled with the lowest Fo content (88.9) and spinel Cr# (8.4). In addition, this sample has the highest La/Yb ratios and U and Th contents in both clinopyroxene and orthopyroxene in the suite (Fig. 4). All these signatures of sample CAM-022 can be explained by modal metasomatism by carbonated silicate melt that converts orthopyroxene to clinopyroxene and olivine (e.g., Gervasoni et al., 2017).

In contrast, the rest of the Nyos suite has major element compositions and mineral modal abundances consistent with the results of melt extraction modeling. Thus, we consider that the remainder of our Nyos peridotites did not suffer substantial modal metasomatism. As mentioned above, both clinopyroxene and orthopyroxene have LREE contents that are too high to be accounted for by melt depletion only. Moreover, both pyroxenes have elevated U and Th concentrations relative to their surrounding elements in the spider diagram (Fig. 4b). This is also observed in many Nyos clinopyroxenes reported in prior studies (Fig. S5; Lee et al., 1996; Temdjem, 2012; Pintér et al., 2015; Liu et al., 2017) and global peridotite clinopyroxenes. Such enrichment and alteration has been ascribed to multiple metasomatic agents ranging from silicate melts (Zangana et al., 1999), aqueous or CO₂-rich fluids (O'Reilly and Griffin, 1988; Downes, 2001) to carbonated melts (Rudnick et al., 1993; Yaxley et al. 1998; Shu and Brey, 2015), acting individually or in combination. Carbonated melts are normally characterized by higher LREE and Eu contents but lower high field strength element (HFSE including Ti, Zr, Hf, Nb, Ta) contents than silicate melts. From the spider diagrams, it is seen that clinopyroxene is commonly depleted in HFSE and relatively enriched in LREE. On the other hand, orthopyroxene has significant amounts of HFSE as shown by the spikes of positive anomalies (Fig. 4b; Fig. S5). Clinopyroxene is the dominant phase hosting REE, particularly MREE to LREE, while

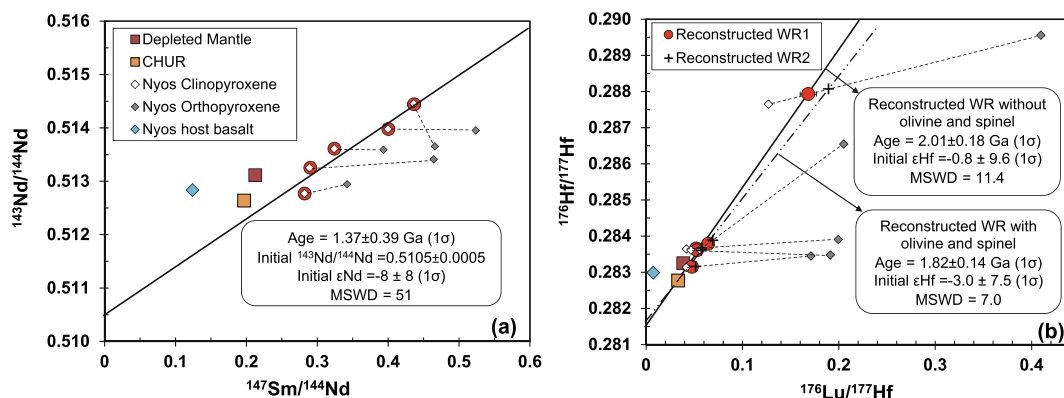


Fig. 8. (a) Sm-Nd isochron and (b) Lu-Hf isochron diagrams of both clinopyroxene and orthopyroxene of the Nyos peridotites examined here as well as the reconstructed whole-rock compositions that are calculated in two ways: WR1 from measured pyroxenes assuming that the other phases contain negligible amounts of these elements in these spinel facies peridotites, and WR2 from all peridotitic minerals assuming that all the phases plot on the two pyroxene isochron trend for each individual peridotite, while trace elemental abundances of both olivine and spinel are calculated using the partition coefficients reported in literature (see details in the Electronic Annex EA-2 Table S4). Also shown are data of the CHUR (Bouvier et al., 2008), Depleted Mantle (Nowell et al., 1998; Bouvier et al., 2008) and the measured host basalt for the Nyos peridotites.

orthopyroxene can contain a significant amount of HREE (e.g., orthopyroxene Yb = 0.16–0.27 ppm (7.3–30% of the whole rock budget) versus clinopyroxene 0.95–2.01 ppm) and HFSE. Therefore, Ti/Eu in clinopyroxene is an underestimate to the bulk value, while La/Yb slightly overestimates the bulk value. Given the potential contamination of the xenoliths by host basalts (e.g., high Ti contents were found at grain boundaries in peridotites; [Byerly and Lassiter, 2015](#)), it is important to reconstruct the whole-rock compositions using two pyroxenes, with the assumption that spinel and olivine contain none of the trace elements considered (Fig. S6); we will discuss below the potential effects of olivine and spinel to the trace element budget. The reconstructed whole-rock values of the studied Nyos peridotites show a relatively low La/Yb and high Ti/Eu that primarily plots within the range of silicate melt metasomatism or melt depletion (Fig. S7) that is also reported in prior studies ([Temdjam, 2012](#); [Pintér et al., 2015](#); [Liu et al., 2017](#)). In addition, both silicate melt and fluid inclusions were observed in some Nyos clinopyroxenes ([Liu et al., 2017](#)) indicating the infiltration of hydrous silicate melts in the SCLM beneath this region of the CVL. However, the high La/Yb and low Ti/Eu signatures of three Nyos harzburgites reported in [Liu et al. \(2017\)](#) are interpreted to reflect the infiltration of carbonated melts (Fig. S7). Considering that orthopyroxene hosts a significant portion of HREE and Ti, the La/Yb and Ti/Eu ratios in clinopyroxene from clinopyroxene-poor and orthopyroxene-rich harzburgites would deviate from the bulk composition ([Scott et al., 2016](#)). Thus, it remains unclear whether these three harzburgites indeed have bulk high La/Yb but low Ti/Eu, when the orthopyroxene composition is not determined. Nonetheless, modal metasomatism by carbonated silicate melt is suggested to have affected sample CAM-022 in our suite as discussed above, which is consistent with the occurrence of carbonated (silicate) melt metasomatism documented previously. Collectively, the Nyos SCLM has been affected to various extents by multiple kinds of metasomatism that is dominated by silicate melts.

5.2. Age of melt depletion and the effects of metasomatism

5.2.1. Re-Os isotope system

Unlike the daughter products of most radiometric couples used to study Earth's mantle, Os, a highly siderophile element, behaves as a compatible element during mantle melting and has a strong affinity to base metal sulfides and alloys in peridotites (e.g., [Hart and Ravizza, 1996](#); [Burton et al., 2000](#); [Brenan et al., 2016](#)). Rhenium behaves like a moderate incompatible element during mantle melting, and it is mainly hosted by base metal sulfides in fertile, sulfide-saturated peridotites, while almost completely excluded in refractory, sulfide-poor peridotites (e.g., [Burton et al., 2002](#); [Fonseca et al., 2007](#); [Brenan et al., 2016](#)). Thus, it is critical to investigate the composition and abundance of sulfides that can be affected by metasomatic or surficial processes and to evaluate their influence on the HSE abundances and possibly Os isotopic composi-

tions of the rocks (e.g., [Alard et al., 2000](#); [Luguet and Pearson, 2019](#)).

Secondary effects on sulfide and HSE systematics: Two forms of sulfides are observed in the Nyos peridotites. Tiny (<10 µm) iron and nickel MSS within the olivine or orthopyroxene grains in the Nyos peridotites (Fig. 2b) are normally interpreted to be residues formed during mantle melt depletion ([Lorand and Luguet, 2016](#)). However, other forms of sulfides can reside in larger complex mineral assemblages (50–200 µm) (Fig. 2c,d). Microscopic observation, quantitative analyses and X-ray elemental mapping reveal an assemblage of pentlandite and chalcopyrite (Electronic Annex EA-2 Table S2) with disseminated Fe-rich phases including small lamellae of native Fe metal (<10 µm) at grain edges (Fig. 2e-i). The Fe-rich phases can contain variable amounts of other elements such as Si, Mg and Ni with FeO ranging from 27.5 to 85.4 wt.%, SiO₂ from 3.4 to 38 wt.%, NiO from 0.3 to 10.8 wt.%, MgO from 0 to 11 wt.%, and SO₃ from 0 to 1.3 wt.% (Electronic Annex EA-2 Table S2). The Fe-rich phases are composed of two end-members: Si-poor and Si-rich phases. The negative trend of FeO versus SiO₂ contents defines a Si-poor endmember with an FeO of ~80% coupled with a NiO of a few percent (Fig. S8). Considering that the totals of the major element oxides analyzed for these phases are generally between 76 and 85 wt.% (Electronic Annex EA-2 Table S2; Fig. S8), we speculate that the Si-poor endmember is composed of Fe-Ni hydroxides, and the Si-rich end-member was derived from Mg-poor silicate melts, but unlikely from Mg-rich host minerals (olivine or orthopyroxene; Fig. 2). The petrographic and geochemical evidence suggests that the mantle sulfides were likely affected by S-undersaturated metasomatic silicate melts that caused sulfide breakdown/dissolution and the formation of complex mineral assemblages consisting of residual pentlandite and chalcopyrite with disseminated Fe-rich phases.

At mantle temperatures, MSS contain significant amounts of copper that leads to Cu-rich liquids when incongruent melting occurs. Copper-rich liquids, which are able to migrate at the grain boundaries, form an intermediate solid solution (Iss) as a phase on the liquidus at about 970 °C, which is the precursor of chalcopyrite ([Harvey et al., 2016](#) and reference therein). Since high T Cu-sulfides contain significant amounts of Ni, pentlandite can exsolve directly as coarse blebs enhanced at chalcopyrite grain boundaries, which is consistent with the observation of sulfide petrology. Thus, alternatively, the Nyos peridotites may have experienced exsolution of sulfides in the mantle. Here we refer sulfide breakdown/dissolution or exsolution to desulfurization. The feature of desulfurization is strongly supported by the sulfide-poor nature, and extremely low bulk S contents of these Nyos peridotites that are far below the values predicted from modeling the effects of melt depletion (Fig. 3b). The fresh nature of these rocks indicates that desulfurization was not likely caused by surficial weathering or serpentinization but occurred at mantle depths.

The Nyos peridotites exhibit typical convex-up HSE patterns characterized by variable, prominent Os, Pd, and

Re depletions relative to Ir (Fig. 5; Liu et al., 2017; this study). Although Pt, Pd, and Re are incompatible and Os, Ir and Ru behave as compatible elements during mantle partial melting (e.g., Pearson et al., 2004; Aulbach et al., 2016), the limited degrees of melt depletion occurring in the Nyos lherzolites from this study and the study of Liu et al. (2017) cannot adequately account for the low Pd_N/Ir_N ratios in these rocks (Fig. 6). Moreover, at the modest level of melt depletion observed in our suite, there should be no significant inter-element variations between Os, Ir and Ru as observed in orogenic massif peridotites and some peridotite xenoliths (e.g., Hannuoba, China; Fig. 6). Instead, such fractionated HSE characteristics are often observed in global post-Archean xenolithic peridotites (e.g., Sidamo, Ethiopia, Lorand et al., 2003a; Penglai, China, Chu et al., 2009; Yangyuan, China, Liu et al., 2010; Kilbourne Hole, Rio Grande Rift, Harvey et al., 2015; Nuomin, Northeast China, Zhang et al., 2019). These features have been explained by desulfurization through metasomatic melt–rock reaction during S-undersaturated conditions or during surficial oxidizing weathering (Lorand et al., 2003b; Lorand and Luguet, 2016). As discussed above, the sulfide petrography and geochemistry of the Nyos peridotites provide excellent evidence for desulfurization during S-undersaturated silicate melt infiltration in the mantle. To investigate the process of desulfurization in controlling the HSE abundances, partial desulfurization of Fe-Ni-Cu sulfides was carried out by Peregoedova et al. (2004). These experiments revealed that Ir–Ru–Pt could be largely retained in the peridotites by forming (Fe)-Pt–Ir alloys (as native Fe is observed in the complex mineral assemblages discussed above; Fig. 2) or hosted by remnant sulfides, whereas Os, Pd and Re would be partially rejected from the Pt–Ir alloys and thus depleted in the bulk rocks, although Os was not specifically examined in the experiments. This type of behaviour can well explain the HSE characteristics of the Nyos peridotites (Fig. 6). The contrasting HSE signatures between xenolithic peridotites and massif peridotites in post-Archean regions led to the suggestion that the volcanic activity, particularly the host magmatism, was the main cause for desulfurization in xenolithic peridotites (Liu et al., 2010). As such, the Nyos peridotites were affected by desulfurization, most likely during or immediately before the eruption (see more chronologic details below). Given the lack of correlation of 1/Os or Os_N/Ir_N and $^{187}Os/^{188}Os$, this process modified the elemental HSE ratios but did not significantly change the Os isotopic composition as it is a process of Os removal, with no addition of Os.

Re-Os dating: As discussed above, recent desulfurization caused loss of both Re and Os. Of note, the Nyos peridotites define a very old apparent isochron age of 3.3 Ga (Fig. 7a). This old age is inconsistent with the high initial $^{187}Os/^{188}Os$ that corresponds to a model age of only ~1.6 Ga. This suggests that the loss of Re is proportionally more than Os, lowering Re/Os and thus steepening the isochron. Although Re/Os has been modified in the process of desulfurization (Figs. 6b, 7a), alumina remains immobile during this process and can be used as a proxy of pristine Re/Os to construct a pseudo-isochron with $^{187}Os/^{188}Os$

(Reisberg and Lorand, 1995; Handler et al., 1997). In the study of Liu et al. (2017), the alumina- $^{187}Os/^{188}Os$ pseudo-isochron is extrapolated to the point of $Al_2O_3 = 0.7\%$, below which no rhenium is believed to be retained in the peridotite residue (Handler et al., 1997), to yield an initial $^{187}Os/^{188}Os$ of 0.1106 that gives a T_{RD} age of 2.6 Ga (if using PUM as the mantle reference line) or 2.4 Ga (if using the ordinary chondrite reservoir that will be applied in this study as a median value between PUM and CI-chondrites) (Fig. 7b). This pseudo-isochron age is significantly older than the oldest T_{RD} ages (2.0 Ga) of the four harzburgites (Liu et al., 2017). Incorporation of our less depleted lherzolite samples in the alumina- $^{187}Os/^{188}Os$ pseudo-isochron of the Nyos peridotites generates variable initial $^{187}Os/^{188}Os$ values that would yield 1.2–2.4 Ga age estimates (Fig. 7b). If the Nyos peridotites were formed in the Archean as claimed by Liu et al. (2017), it would be difficult to explain (1) the variable range of fertile to moderate refractory composition observed in the Nyos peridotites that contrasts strongly with typical refractory Archean peridotites that were formed after high degrees of mantle partial melting (Pearson and Wittig, 2014), and (2) the absence of Archean T_{RD} ages are found in the Nyos peridotites, whereas nearly all suites of Archean cratonic peridotites have a dominant population with T_{RD} ages >2.5 Ga (Carlson et al., 1999; Pearson and Wittig, 2014). Given those aforementioned factors potentially contributing uncertainties when using the Re-Os isotope system to constrain the age of melting in post-Archean peridotites, additional chronologic information from the Lu-Hf system provides a useful perspective.

5.2.2. Sr-Nd-Hf isotope systems

Since Sr isotopic ratios of orthopyroxene from the Nyos peridotites are not available due to the very low concentrations of Sr, this does not permit comparison of Sr isotopic compositions between orthopyroxene and clinopyroxene in these rocks. Although clinopyroxene, as the dominant host of both Sr and Nd, has lower $^{87}Sr/^{86}Sr$ ratios than that of the host basalt measured in this study and other Cameroon basalts (Fig. 9a; e.g., Ballentine et al., 1997), samples CAM-111 and NY-01 from Liu et al. (2017) significantly deviate from the depleted MORB mantle trend (Fig. 9a), implying that their compositions might have been modified by the diversity of metasomatism experienced by these rocks, if the pristine mantle peridotites evolve along the mantle trend. Since $^{87}Sr/^{86}Sr$ ratios of the depleted samples CAM-111 and NY-01 are much higher than the values extrapolated to their $^{143}Nd/^{144}Nd$ values on the MORB mantle trend, the deviation of these two samples can be explained by a recent, significant addition of radiogenic Sr that had relatively less effect on the Nd isotopic composition.

Although all the Nyos peridotites probably experienced metasomatism to variable extents based on their mineral REE patterns and trace element spider diagrams (Fig. 4a, b), log orthopyroxene/clinopyroxene REE ratios are linearly correlated with the X^{3+} ionic radii from Lu to Sm, indicating that for these elements equilibrium existed

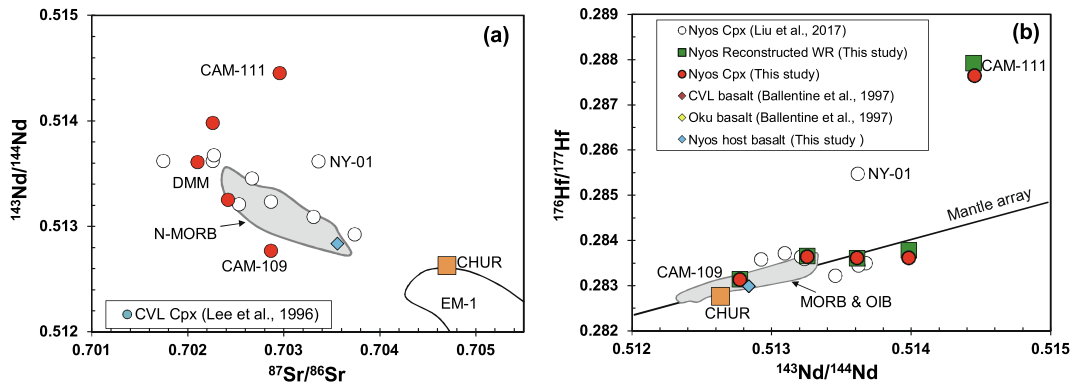


Fig. 9. (a) $^{143}\text{Nd}/^{144}\text{Nd}$ versus $^{87}\text{Sr}/^{86}\text{Sr}$ and (b) $^{176}\text{Hf}/^{177}\text{Hf}$ versus $^{143}\text{Nd}/^{144}\text{Nd}$ of both clinopyroxene and orthopyroxene of the Nyos peridotites examined here, as well as the reconstructed whole-rock compositions. Also shown are the literature data including cpx from the CVL peridotites (Lee et al., 1996) and the Nyos peridotites (Liu et al., 2017), as well as the CVL basalts (Ballentine et al., 1997). N-MORB: Hofmann (2014); MORB & OIB: Stracke et al. (2011); the mantle array: Vervoort and Blichert-Toft (1999).

between the two types of pyroxenes under mantle conditions, while some significant scatter/elevation is observed from Nd to La (Fig. 4c). The equilibrium of Lu to Sm in coexisting orthopyroxene and clinopyroxene can be used to calculate the REE equilibrium temperatures ($T_{\text{REE}} = 926\text{--}1043\text{ }^{\circ}\text{C}$; Table 1) that are generally consistent with the two-pyroxene thermometer data ($T_{\text{BKN}} = 942\text{--}1065\text{ }^{\circ}\text{C}$; Table 1) calculated based on major element compositions that are less sensitive to cryptic metasomatism. With regards to the scatter/elevation from Nd to La, although there are relatively large uncertainties in the measurements of these extremely low concentrations of LREE in orthopyroxene (Table 5), the observed scatter for these elements is beyond analytical uncertainty. We speculate that the scatter from Nd to La is mainly caused by the disequilibrium effects of metasomatism on these elements that are poorly concentrated in pyroxenes (see more discussion based on Nd isotopes below) as well as their low diffusivities.

Calculated equilibrium temperatures are well above the closure temperature of Nd isotopes in pyroxenes ($\sim 850\text{ }^{\circ}\text{C}$; Shu et al., 2014), which means that the Nd isotopic composition of the pyroxene pairs should be identical if equilibrium existed before eruption. In reality, there are several scenarios in the pyroxene pairs of the five analyzed Nyos peridotites (Fig. 8a; Table 5). For instance, samples CAM-020 and CAM-108 have identical $^{143}\text{Nd}/^{144}\text{Nd}$ in coexisting orthopyroxene and clinopyroxene, which indicates equilibration of Nd isotopes in this mineral pair, consistent with their high equilibrium temperatures. In contrast, the orthopyroxene in samples CAM-102b and CAM-109 have $^{143}\text{Nd}/^{144}\text{Nd}$ somewhat higher than their co-existing clinopyroxene, generating two-point isochron ages of $140 \pm 62\text{ Ma}$ and $439 \pm 150\text{ Ma}$, respectively (Table 5), and these ages are significantly older than the eruption age of host basalts ($1.1\text{--}3.5\text{ Ma}$; Freeth and Rex, 2000). This may indicate that the sampled lithospheric mantle experienced rapid uplift to shallower depths in the past without significantly resetting the REE partitioning between the pyroxene pairs. Exceptionally, the orthopyroxene of sample CAM-111 has a lower

$^{143}\text{Nd}/^{144}\text{Nd}$ than its coexisting clinopyroxene, giving a negative two-point isochron age (Table 5). This inconsistency with their Sm/Nd ratios is best explained by recent metasomatic alteration that influenced more the extremely Nd-poor orthopyroxene than clinopyroxene. This process most likely occurred during or shortly before eruption from the contamination of host basaltic lava, which can potentially account for the variable Sr-Nd isotope compositions of the Cameroon peridotitic clinopyroxenes (Fig. 9a; Liu et al., 2017), and did not allow sufficient time to equilibrate Nd isotopes in pyroxenes. This also coincides with recent desulfurization as discussed above. In addition, sample CAM-111 shows a significant decoupling between Nd and Hf isotopes (i.e., lower $^{143}\text{Nd}/^{144}\text{Nd}$ compared to $^{176}\text{Hf}/^{177}\text{Hf}$) when normalized to the mantle array, while the other samples plot within or close to the mantle array (Fig. 9b). Therefore, CAM-111 may also have undergone significant alteration of Nd isotopes in addition to Sr isotopes mentioned above, consistent with it having a more elevated Nd concentration than predicted from melt modeling (Fig. 4). Collectively, it is evident from the Nyos suite that the extent of metasomatic modification is greatest in the order of $\text{Sr} > \text{Nd} > \text{Hf}$ isotopes, as suggested by previous studies (e.g., Scherer et al., 2000; Ionov et al., 2005; Wittig et al., 2006; Liu et al., 2012; Shu et al., 2013; Byerly and Lassiter, 2015). Given the observed metasomatic enrichment of Nd isotopes, the Nd model ages of these peridotites should underestimate melt depletion ages and can be treated as a lower limit constraint of the peridotite formation age. Since clinopyroxene dominates the budget of Sm and Nd, the Sm-Nd isotope system in clinopyroxene (or reconstructed whole-rock) is more robust than orthopyroxene in retaining primary melt depletion signatures (Table 5). As such, the Nyos peridotites experienced melt depletion by at least 0.9 Ga (maximum $T_{\text{DM}}(\text{Nd})$) or 1.2 Ga (maximum $T_{\text{CHUR}}(\text{Nd})$), consistent with previous results (Lee et al., 1996). This is also supported by the reconstructed whole-rock or clinopyroxene isochron age ($1.37 \pm 0.39\text{ Ga}$ (1σ); Fig. 8a), although the large scatter ($\text{MSWD} = 51$) also reflects alteration by secondary metasomatism.

Unlike Nd isotopes, the Lu-Hf isotope system yields more consistent results. Nyos peridotite orthopyroxenes have $^{176}\text{Hf}/^{177}\text{Hf}$ identical to, or significantly higher, than their coexisting clinopyroxenes. This is consistent with the estimated higher closure temperature ($\sim 920^\circ\text{C}$) of the Lu-Hf isotope system in pyroxenes (Shu et al., 2014). A further implication is that Hf isotopes are not necessarily at isotopic equilibrium in pyroxene pairs in peridotites. Considering the potentially more vulnerable status of Hf isotopes in orthopyroxene (characterized by high Lu/Hf but low Hf content) compared to clinopyroxene (characterized by low Lu/Hf but high Hf content) and the diffusive exchange of Hf isotopes between the pair, a two-point isochron age can be treated as the minimum estimate for the age of peridotites. The two-point isochron ages for the Nyos peridotites are variable and range from around zero to 1.0 Ga, which indicates that the Nyos peridotites were formed at least 1 Ga.

Additional evidence indicates a much greater antiquity to the melting event. Hafnium model ages ($T_{\text{DM}}(\text{Hf}) = 1.1\text{--}1.9\text{ Ga}$, and $T_{\text{CHUR}}(\text{Hf}) = 1.4\text{--}2.5\text{ Ga}$) calculated using the reconstructed whole-rock isotope compositions are significantly older than the two-point isochron “cooling ages”. Orthopyroxene controls up to 33% Lu and 14% Hf in the whole rock budget. This proportion increases through progressive melt extraction (Fig. S9). Hence, to further constrain the formation age of the Nyos peridotites, it is necessary to reconstruct a whole-rock Lu-Hf isochron combining data of both clinopyroxene and orthopyroxene. Such an isochron yields an age of $2.01 \pm 0.18\text{ Ga}$ (1σ) with an initial ε_{Hf} of $-0.8 \pm 9.6\text{ (1}\sigma)$ (Fig. 8b). Furthermore, melt modeling calculations show that olivine hosts up to 16% of Lu and 5% of Hf in the whole rock budget, while spinel likely contains negligible Lu and Hf (Fig. S9). Due to too low Hf abundances, neither olivine nor spinel was measured for the Lu-Hf isotopic compositions. We assume that the Lu-Hf isotopic compositions of olivine and spinel plot on the isochron trend defined by the two pyroxenes for each individual peridotite, through which the whole-rock Lu-Hf isotopic composition can be reconstructed using all the major peridotitic phases. As a result, the reconstructed whole-rock isochron using all the peridotitic phases gives an age of $1.82 \pm 0.14\text{ Ga}$ (1σ) with an initial ε_{Hf} of $-3.0 \pm 7.5\text{ (1}\sigma)$ (Fig. 8b). Both ages are identical within error, indicating that olivine has some effect but is not the dominant control on the whole-rock Lu-Hf isochron of peridotites. The reconstructed whole-rock isochron age has a much higher precision than the age ($2.65 \pm 0.72\text{ Ga}$) recorded by constructing an isochron clinopyroxene alone. The reconstructed whole-rock isochron is in better agreement with the regional geological constraints on the evolution of the crust in this region. This result demonstrates the necessity of measuring the isotope compositions of both orthopyroxene and clinopyroxene (as well as garnet if present), enabling reconstruction of a whole-rock isochron to better determine the melt depletion age of the peridotites. Moreover, the initial ε_{Hf} value from the reconstructed whole-rock isochron is identical within uncertainty to the depleted mantle or chondritic mantle, in contrast to large positive initial ε_{Hf} values derived from clinopyroxene

isochrons in previous studies (Choi et al., 2008, 2010; Liu et al., 2012) that have been ascribed to isotopic exchange with coexisting higher-Lu/Hf orthopyroxene, as evidenced by the young two-point isochron ages in this study (Table 5).

What does the reconstructed whole-rock Lu-Hf isochron age date? If the parent-daughter elemental fractionation was established during melt extraction of the mantle and the isotope system remains close since then, the isochron age will date the melt depletion of peridotites and therefore formation of the lithospheric mantle. However, modeling calculations show that the reconstructed whole-rock Lu/Hf ratios of the Nyos peridotites are normally lower than those expected from non-modal fractional melting (Fig. S4b), which indicates enrichment of Hf over Lu through ancient (e.g., right after melt extraction) or recent metasomatism. We propose that the Nyos peridotites most likely experienced metasomatic enrichment right after melt extraction through upward infiltration of remnant silicate-dominated melts, based on the following reasons: (1) the two-point Lu-Hf isochron ages of the Nyos peridotites are normally around zero to positive with a maximum of ca. 1.0 Ga; (2) Hf model ages ($T_{\text{DM}}(\text{Hf}) = 1.1\text{--}1.9\text{ Ga}$, and $T_{\text{CHUR}}(\text{Hf}) = 1.4\text{--}2.5\text{ Ga}$) are older than the maximum two-point isochron age; and (3) the reconstructed whole-rock Lu-Hf isochron age lies in the range of alumina- $^{187}\text{Os}/^{188}\text{Os}$ pseudo-isochron ages (1.2–2.4 Ga; Liu et al., 2017; this study), and in fact agrees exactly with the oldest of the T_{RD} ages (2.0 Ga) of these rocks. This can well explain the decoupling of the reconstructed whole-rock $^{176}\text{Hf}/^{177}\text{Hf}$ versus measured whole-rock $^{187}\text{Os}/^{188}\text{Os}$ of sample CAM-102b (Fig. S10) that has significantly lower Lu/Hf and $^{176}\text{Hf}/^{177}\text{Hf}$ but a similar $^{187}\text{Os}/^{188}\text{Os}$ compared to those of sample CAM-111 (Table 4, Table 5), although both samples have similar major element compositions ($\text{Al}_2\text{O}_3 = 2.44\text{ wt.\%}$ vs. 2.01 wt.\% ; $\text{Fo} = 91.1$ vs. 91.2 ; $\text{Cr\#} = 17.5$ vs. 19.3). In addition, although the Nyos host basalt plots at one endmember of the $^{176}\text{Hf}/^{177}\text{Hf}$ vs. $1/\text{Hf}$ diagrams (Fig. S11), the host basalt did not significantly alter the Lu/Hf isotopic composition of the leached mineral separates of the Nyos peridotites. Collectively, although ancient incipient metasomatism affected the Nyos peridotites, the whole-rock Lu-Hf isotope system in these spinel facies lherzolites appear to have remained faithful tracers of the melt-depletion history of the SCLM.

Overall, we conclude that the SCLM sampled by the Nyos peridotites was formed at $\sim 2.0\text{ Ga}$, rather than in the Archean (Liu et al., 2017). As demonstrated by the Nyos peridotites in this study, the reconstructed whole-rock Lu-Hf isotope system can be used in well-preserved fresh spinel-facies peridotites (and also garnet-facies peridotites from which clinopyroxene, orthopyroxene and garnet should be individually measured) to obtain the most accurate estimate age of melt depletion, although they may have experienced metasomatic enrichment right after melt extraction. When this is done, the Lu-Hf decay system is a radiometric tool complementary to the Re-Os isotope system for dating post-Archean peridotites (e.g., Wittig et al., 2006; Pearson and Wittig, 2014). For those peridotites that were highly metasomatized in the later

evolutionary history, the Re-Os isotope system may still provide better age constraints of melt depletion than other radiometric dating systematics.

5.3. Tectonic implications for the Cameroon continental sector and origin of CVL

The Nyos area is located in the Western Cameroon Domain within the Central African Fold Belt (Fig. 1). Although there is a considerable amount of juvenile Neoproterozoic crust found in this domain (Toteu et al., 2004), the characteristics of basement rocks at or near the Nyos area are not well known, as voluminous CVL mantle magmatism occurs on the surface (Fig. 1). Of note, fragments of ~2.1 Ga crust units were identified in the Western Cameroon Domain (Toteu et al., 2001, 2004). The finding of Paleoproterozoic crust in this domain is consistent with the recognition of ~2.0 Ga SCLM in the Nyos area. To date, there is no evidence of Archean crust found in this area. Thus, our data imply that the Western Cameroon Domain formed a Paleoproterozoic mantle root that has been extant since that time. Although the Central Cameroon–Tcholliré–Banyo shear zones have been used to define the boundary of the Western Cameroon Domain and the Paleoproterozoic Adamawa–Yadé Domain (Toteu et al., 2001, 2004), the suture at mantle depths is not well defined. Considering that the Nyos area lies <80 km away from the Central Cameroon–Tcholliré–Banyo shear zones (Fig. 1), it is also possible that the SCLM sampled by the Nyos peridotites may represent fragments of the SCLM from the Paleoproterozoic Adamawa–Yadé Domain through collisional emplacement during the Pan African Orogeny. Given the large variation and even disagreement among the limited isotope data from mantle xenoliths from the Cameroon continental sector and beyond in the CVL (Lee et al., 1996; Liu et al., 2017; this study), extensive radiometric dating of other mantle peridotites from this region, especially to the west and south of the Nyos area, is needed to better define the age structure of the lithospheric root and to ascertain with more confidence whether there are any Archean components to the root.

With regards to the origin of the CVL, our data demonstrate that the infiltration of host basalts strongly influenced the Nyos peridotites. Although melting of a potential mixture of the observed SCLM components could possibly account for the Sr-Nd isotope composition of the CVL basalts (Fig. 9a), the Hf isotopic compositions of the Nyos peridotites are too radiogenic to allow these rocks to be the main source of the CVL basalts (Fig. 9b; Liu et al., 2017; this study). This is consistent with the recognition that the CVL primarily resulted from reactivation of lithospheric shear zones tapping sub-lithospheric mantle (Fitton, 1987; Meyers et al., 1998; Déruelle et al., 2007; Assah et al., 2015).

6. CONCLUSIONS

Data for relatively immobile major and trace element data in eight fresh spinel lherzolite xenoliths from Nyos, Cameroon indicate that they are mantle residues of a few percent to <16% melt depletion. However, the trace element

patterns of both clinopyroxene and orthopyroxene reflect the effects of metasomatic enrichment in addition to melt depletion. The relatively low La/Yb and high Ti/Eu ratios of the reconstructed bulk rocks are consistent with silicate melt metasomatism. Some orthopyroxenes have lower $^{143}\text{Nd}/^{144}\text{Nd}$ than coexisting clinopyroxenes, which is best explained by recent rapid metasomatic alteration most likely by host basaltic lava. This process also led to desulfurization in the Nyos peridotites, which can account for the observed convex-up HSE patterns. Due to metasomatic disturbance, the Sr-Nd isotope systems in pyroxenes cannot accurately reflect the melt depletion signature. Unlike Sr-Nd isotopes, the Lu-Hf isotope system is more robust to recent metasomatic overprinting. Given that orthopyroxene controls up to 33% Lu and 14% Hf in the whole rock budget and has $^{176}\text{Hf}/^{177}\text{Hf}$ ratios similar to, or higher than those of coexisting clinopyroxene, it is necessary to reconstruct a whole-rock Lu-Hf isochron in order to constrain the melt depletion age and the initial Hf isotopic ratio of the peridotites. The resulting reconstructed whole-rock Nyos Lu-Hf isochron from ortho- and clinopyroxenes gives an age of 2.01 ± 0.18 (1 σ) with an initial ϵ_{Hf} of -0.8 ± 9.6 (1 σ) and when olivine and spinel are considered, is 1.84 ± 0.14 (1 σ) with an initial ϵ_{Hf} of -3.0 ± 7.5 (1 σ). These two ages are identical within error, and they are also within error of the alumina- $^{187}\text{Os}/^{188}\text{Os}$ pseudo-isochron ages (1.2–2.4 Ga; Liu et al., 2017; this study), and is consistent with the oldest rhenium depletion Os model ages (2.0 Ga) of the four Nyos harzburgites reported in Liu et al. (2017). We conclude that the Nyos peridotite suite, and the continental mantle root that they derive from, was formed by melt depletion at ~2.0 Ga. This result illustrates clearly how reconstructed whole-rock Lu-Hf isotope systematics can be a powerful radiometric tool that is complementary to the Re-Os isotope system in dating well-preserved post-Archean peridotites, even in peridotites that may have experienced metasomatic enrichment right after melt extraction. The recognition of ~2.0 Ga SCLM in the Nyos area suggests that the Nyos region assembled as a Paleoproterozoic block, or these Nyos peridotites may represent fragments of the SCLM from the nearby Paleoproterozoic domain displaced by collision during the Pan African Orogeny. With regards to the origin of the CVL, our data reveal that the Hf isotopic compositions of the Nyos peridotites are too radiogenic to be the main source of the CVL basalts, which is consistent with derivation of these magmas from the sub-lithospheric mantle during reactivation of lithospheric shear zones.

ACKNOWLEDGEMENTS

This work was supported by funding from the Canada Excellence Research Chairs program to DGP and the National Natural Science Foundation of China (No. 41822301, 41790451, 41730214), China “1000 Youth Talents Program” and the 111 project (B18048) to JL. We thank Martin von Dollen for preparing the thin sections, Andrew Locock for providing assistance in the EMPA analyses, Yan Luo, Sarah Woodland and Chiranjeeb Sarkar for help in the lab, and Chuanzhou Liu, Gongcheng Tian and Ronghua Cai for discussion. Special thanks go to Prof. Roberta Rudnick who supervised and mentored JL to make his career

possible. Executive Editor Jeffrey Catalano, Associate Editor Fang-Zhen Teng, Guest Editor Sonja Aulbach, and reviewers Michael Bizimis, Laurie Reisberg, and John Lassiter are thanked for handling and providing comments that significantly improved the quality of this manuscript. This is CUGB petro-geochemical contribution no. PGC2015-0042 (RIG-no.3).

APPENDIX A. SUPPLEMENTARY MATERIAL

Supplementary data to this article can be found online at <https://doi.org/10.1016/j.gca.2019.07.010>.

REFERENCES

- Ackerman L., Bizimis M., Haluzová E., Sláma J., Svojtka M., Hirajima T. and Erban V. (2016) Re–Os and Lu–Hf isotopic constraints on the formation and age of mantle pyroxenites from the Bohemian Massif. *Lithos* **256–257**, 197–210.
- Alard O., Griffin W. L., Lorand J. P., Jackson S. E. and O'Reilly S. Y. (2000) Non-chondritic distribution of the highly siderophile elements in mantle sulphides. *Nature* **407**, 891.
- Assah A. N. E., Yokoyama T., Aka F. T., Usui T., Wirmvem M. J., Tchamabe B. C., Ohba T., Tanyileke G. and Hell J. V. (2015) A comparative review of petrogenetic processes beneath the Cameroon Volcanic Line: Geochemical constraints. *Geosci. Front.* **6**, 557–570.
- Aulbach S., Mungall J. E. and Pearson D. G. (2016) Distribution and processing of highly siderophile elements in cratonic mantle lithosphere. *Rev. Mineral. Geochem.* **81**, 239–304.
- Ballentine C. J., Lee D. C. and Halliday A. N. (1997) Hafnium isotopic studies of the Cameroon Line and new HIMU paradoxes. *Chem. Geol.* **139**, 111–124.
- Becker H., Horan M. F., Walker R. J., Gao S., Lorand J. P. and Rudnick R. L. (2006) Highly siderophile element composition of the Earth's primitive upper mantle: constraints from new data on peridotite massifs and xenoliths. *Geochim. Cosmochim. Acta* **70**, 4528–4550.
- Bernstein S., Kelemen P. B. and Hanghøj K. (2007) Consistent olivine Mg# in cratonic mantle reflects Archaean mantle melting to the exhaustion of orthopyroxene. *Geology* **35**, 459–462.
- Bizimis M., Sen G. and Salters V. J. M. (2004) Hf–Nd isotope decoupling in the oceanic lithosphere: constraints from spinel peridotites from Oahu Hawaii. *Earth Planet. Sci. Lett.* **217**, 43–58.
- Boyd F. R. and Mertzman S. A. (1987) *Composition of structure of the Kaapvaal lithosphere southern Africa*. The Geochemical Society Special Publication, p. 1.
- Bouvier A., Vervoort J. D. and Patchett P. J. (2008) The Lu–Hf and Sm–Nd isotopic composition of CHUR: constraints from unequilibrated chondrites and implications for the bulk composition of terrestrial planets. *Earth Planet. Sci. Lett.* **273**, 48–57.
- Brenan J. M., Bennett N. R. and Zajacz Z. (2016) Experimental results on fractionation of the Highly Siderophile Elements (HSE) at variable pressures and temperatures during planetary and magmatic differentiation. *Rev. Mineral. Geochem.*, 1–87.
- Brey G. P. and Köhler T. (1990) Geothermobarometry in four-phase Iherzolites II. New thermobarometers, and practical assessment of existing thermobarometers. *J. Petrol.* **31**, 1353–1378.
- Burton K. W., Capmas F., Birck J. L., Allègre C. J. and Cohen A. S. (2000) Resolving crystallization ages of Archean mafic–ultramafic rocks using the Re–Os isotope system. *Earth Planet. Sci. Lett.* **179**, 453–467.
- Burton K. W., Gannoun A., Birck J. L., Allegre C. J., Schiano P., Clocchiatti R. and Alard O. (2002) The compatibility of rhenium and osmium in natural olivine and their behavior during mantle melting and basalt genesis. *Earth Planet. Sci. Lett.* **198**, 63–76.
- Byerly B. L. and Lassiter J. C. (2015) Trace element partitioning and Lu–Hf isotope systematics in spinel peridotites from the Rio Grande Rift and Colorado Plateau: towards improved age assessment of clinopyroxene Lu/Hf- 176 Hf/ 177 Hf in SCLM peridotite. *Chem. Geol.* **413**, 146–158.
- Carlson R. W. and Irving A. J. (1994) Depletion and enrichment history of subcontinental lithospheric mantle—an Os Sr Nd and Pb isotopic study of ultramafic xenoliths from the Northwestern Wyoming Craton. *Earth Planet. Sci. Lett.* **126**, 457–472.
- Carlson R. W., Pearson G., Boyd F. R., Shirey S. B., Irvine G., Menzies A. and Gurney J. (1999) Re–Os Systematics of Lithospheric Peridotites: Implications for Lithosphere Formation and Preservation. In *7th International Kimberlite Conference, Volume I*, pp. 99–108.
- Carlson R. W., Irving A. J., Schulze D. J. and Hearn B. C. (2004) Timing of Precambrian melt depletion and Phanerozoic refertilization events in the lithospheric mantle of the Wyoming Craton and adjacent Central Plains Orogen. *Lithos* **77**, 453–472.
- Choi S. H., Mukasa S. B., Zhou X. H., Xian X. H. and Androniko A. V. (2008) Mantle dynamics beneath East Asia constrained by Sr Nd Pb and Hf isotopic systematics of ultramafic xenoliths and their host basalts from Hannuoba North China. *Chem. Geol.* **248**, 40–61.
- Choi S. H., Suzuki K., Mukasa S. B., Lee J. I. and Jung H. (2010) Lu–Hf and Re–Os systematics of peridotite xenoliths from Spitsbergen western Svalbard: implications for mantle–crust coupling. *Earth Planet. Sci. Lett.* **297**, 121–132.
- Chu Z. Y., Wu F. Y., Walker R. J., Rudnick R. L., Pitcher L., Puchtel I. S., Yang Y. H. and Wilde S. A. (2009) Temporal evolution of the lithospheric mantle beneath the Eastern North China Craton. *J. Petrol.* **50**, 1857–1898.
- Doucet L. S., Ionov D. A. and Golovin A. V. (2015) Paleoproterozoic formation age for the Siberian cratonic mantle: Hf and Nd isotope data on refractory peridotite xenoliths from the Udachnaya kimberlite. *Chem. Geol.* **391**, 42–55.
- Downes H. (2001) Formation and modification of the shallow sub-continental lithospheric mantle: a review of geochemical evidence from ultramafic xenolith suites and tectonically emplaced ultramafic massifs of western and central Europe. *J. Petrol.* **42**, 233–250.
- Déruelle B., Ngounouno S. and Demaiffe D. (2007) The Cameroon hot line (CHL): a unique example of active alkaline intraplate structure in both oceanic and continental lithospheres. *C. R. Geosci.* **339**, 589–600.
- Fitton J. G. (1987) The Cameroon line, West Africa: a comparison between oceanic and continental alkaline volcanism. *Geol. Soc., Lond., Special Publ.* **30**(1), 273–291. <https://doi.org/10.1144/GSL.SP.1987.030.01.13>.
- Fleet M. E., Crocket J. H., Liu M. H. and Stone W. E. (1999) Laboratory partitioning of platinum-group elements (PGE) and gold with application to magmatic sulfide–PGE deposits. *Lithos* **47**, 127–142.
- Fonseca R. O., Mallmann G., O'Neill H. S. C. and Campbell I. H. (2007) How chalcophile is rhenium? An experimental study of the solubility of Re in sulphide mattes. *Earth Planet. Sci. Lett.* **260**(3), 537–548.
- Freeth S. J. and Rex D. C. (2000) Constraints on the age of Lake Nyos Cameroon. *J. Volcanol. Geotherm. Res.* **97**, 261–269.

- Gao S., Rudnick R. L., Carlson R. W., McDonough W. F. and Liu Y. S. (2002) Re–Os evidence for replacement of ancient mantle lithosphere beneath the North China craton. *Earth Planet. Sci. Lett.* **198**, 307–322.
- Gervasoni F., Klemme S., Rohrbach A., Grützner T. and Berndt J. (2017) Experimental constraints on mantle metasomatism caused by silicate and carbonate melts. *Lithos* **282–283**, 173–186.
- Handler M. R., Bennett V. C. and Esat T. M. (1997) The persistence of off-cratonic lithospheric mantle: Os isotopic systematics of variably metasomatised southeast Australian xenoliths. *Earth Planet. Sci. Lett.* **151**, 61–75.
- Harris G. A., Pearson D. G., Liu J., Hardman M. F., Snyder D. B. and Kelsch D. (2018) Mantle composition, age and geotherm beneath the Darby kimberlite field, west central Rae Craton. *Miner. Petrol.* **122**, 57–70.
- Hart S. R. and Ravizza G. (1996) Os partitioning between phases in lherzolite and basalt. *Isotopic Stud. Crust-mantle Evol. AGU Monogr.* **95**, 123–134.
- Harvey J., Konig S. and Luguet A. (2015) The effects of melt depletion and metasomatism on highly siderophile and strongly chalcophile elements: S–Se–Te–Re–PGE systematics of peridotite xenoliths from Kilbourne Hole New Mexico. *Geochim. Cosmochim. Acta* **166**, 210–233.
- Harvey J., Warren J. M. and Shirey S. B. (2016) Mantle sulfides and their role in Re–Os and Pb isotope geochemistry. *Rev. Mineral. Geochem.* **81**, 579–649.
- Herrmann W. and Berry R. F. (2002) MINSQ-a least squares spreadsheet method for calculating mineral proportions from whole rock major element analysis: geochemistry: exploration. *Environ. Anal.* **2**, 361–368.
- Hofmann A. W. (2014) 3.3 - Sampling mantle heterogeneity through oceanic basalts: Isotopes and trace elements. In *Treatise in Geochemistry*, vol. 2 (ed. R. W. Carlson). Elsevier, Amsterdam, pp. 67–101.
- Horan M. F., Walker R. J., Morgan J. W., Grossman J. N. and Rubin A. E. (2003) Highly siderophile elements in chondrites. *Chem. Geol.* **196**, 5–20.
- Irvine G. J., Pearson D. G. and Carlson R. W. (2001) Lithospheric mantle evolution of the Kaapvaal Craton: a Re–Os isotope study of peridotite xenoliths from Lesotho kimberlites. *Geophys. Res. Lett.* **28**, 2505–2508.
- Ionov D. A., Blöcher-Toft J. and Weis D. (2005) Hf isotope compositions and HREE variations in off-craton garnet and spinel peridotite xenoliths from central Asia. *Geochim. Cosmochim. Acta* **69**, 2399–2418.
- Johnson K. T. M., Dick H. J. B. and Shimizu N. (1990) Melting in the oceanic upper mantle—an ion microprobe study of diopside in abyssal peridotites. *J. Geophys. Res.-Solid Earth Planets* **95**, 2661–2678.
- Jugo P., Luth R. W. and Richards J. P. (2005) An experimental study of the sulfur content in basaltic melts saturated with immiscible sulfide or sulfate liquids at 1300°C and 1.0 GPa. *J. Petrol.* **46**(4), 783–798.
- Lazarov M., Brey G. B. and Weyer S. (2009) Time steps of depletion and enrichment in the Kaapvaal craton as recorded by subcalcic garnets from Finsch (SA). *Earth Planet. Sci. Lett.* **27**, 1–10.
- Ledru P., Johan V., Milesi J. P. and Tegey M. (1994) Markers of the last stages of the Paleoproterozoic collision: evidence for a 2 Ga continent involving circum-South Atlantic provinces. *Precamb. Res.* **69**, 169–191.
- Lee C. T., Yin Q. Z., Rudnick R. L., Chesley J. T. and Jacobsen S. B. (2000) Osmium isotopic evidence for mesozoic removal of lithospheric mantle beneath the Sierra Nevada California. *Science* **289**, 1912–1916.
- Lee D.-C., Halliday A. N., Fitton J. G. and Poli G. (1994) Isotopic variations with distance and time in the volcanic islands of the Cameroon line: evidence for a mantle plume origin. *Earth Planet. Sci. Lett.* **123**, 119–138.
- Lee D.-C., Halliday A. N., Davies G. R., Essene E. J., Fitton J. G. and Temdjam R. (1996) Melt enrichment of shallow depleted mantle: a detailed petrological, trace element and isotopic study of mantle-derived xenoliths and megacrysts from the Cameroon Line. *J. Petrol.* **37**, 415–441.
- Liang Y., Sun C. and Yao L. (2012) A REE-in-two-pyroxene thermometer for mafic and ultramafic rocks. *Geochim. Cosmochim. Acta* **102**, 246–260.
- Liu C. Z., Yang L. Y., Li X. H. and Tchouankoue J. P. (2017) Age and Sr–Nd–Hf isotopes of the sub-continental lithospheric mantle beneath the Cameroon Volcanic Line: Constraints from the Nyos mantle xenoliths. *Chem. Geol.* **455**, 84–97.
- Liu J. G., Rudnick R. L., Walker R. J., Gao S., Wu F. Y. and Piccoli P. M. (2010) Processes controlling highly siderophile element fractionations in xenolithic peridotites and their influence on Os isotopes. *Earth Planet. Sci. Lett.* **297**, 287–297.
- Liu J. G., Carlson R. W., Rudnick R. L., Walker R. J., Gao S. and Wu F. Y. (2012) Comparative Sr–Nd–Hf–Os–Pb isotope systematics of xenolithic peridotites from Yangyuany North China Craton: Additional evidence for a Paleoproterozoic age. *Chem. Geol.* **332–333**, 1–14.
- Liu J. and Pearson D. G. (2014) Rapid precise and accurate Os isotope ratio measurements of nanogram to sub-nanogram amounts using multiple Faraday collectors and amplifiers equipped with 10 12 X resistors by N-TIMS. *Chem. Geol.* **363**, 301–311.
- Liu J. G., Scott J. M., Martin C. E. and Pearson D. G. (2015) The longevity of Archean mantle residues in the convecting upper mantle and their role in young continent formation. *Earth Planet. Sci. Lett.* **424**, 109–118.
- Liu J. G., Brin L. E., Pearson D. G., Bretschneider L., Luguet A., van Acken D., Kjarsgaard B., Riches A. and Mišković A. (2018) Diamondiferous Paleoproterozoic mantle roots beneath Arctic Canada: A study of mantle xenoliths from Parry Peninsula and Central Victoria Island. *Geochim. Cosmochim. Acta* **239**, 284–311.
- Lorand J. P. and Luguet A. (2016) Chalcophile and siderophile elements in mantle rocks: trace elements controlled by trace minerals. *Rev. Mineral. Geochem.* **81**, 441–488.
- Lorand J. P., Alard O., Luguet A. and Keays R. R. (2003a) Sulfur and selenium systematics of the subcontinental lithospheric mantle: Inferences from the Massif Central xenolith suite (France). *Geochim. Cosmochim. Acta* **67**, 4137–4151.
- Lorand J. P., Reisberg L. and Bedini R. M. (2003b) Platinum-group elements and melt percolation processes in Sidamo spinel peridotite xenoliths, Ethiopia, East African Rift. *Chem. Geol.* **196**, 57–75.
- Luguet A., Jaques A. L., Pearson D. G., Smith C. B., Bulanova G. P., Roffey S. L., Rayner M. J. and Lorand J. P. (2009) An integrated petrological, geochemical and Re–Os isotope study of peridotite xenoliths from the Argyle lamproite, Western Australia and implications for cratonic diamond occurrences. *Lithos* **112**, 1096–1108.
- Luguet A. and Pearson D. G. (2019) Dating mantle peridotites using Re–Os isotopes: The complex message from whole rocks, base metal sulfides and platinum group minerals. *Am. Mineral.* **104**, 165–189.
- Matsukage K. N. and Oya M. (2010) Petrological and chemical variability of peridotite xenoliths from the Cameroon Volcanic Line West Africa: an evidence for plume emplacement. *J. Mineral. Petrol. Sci.* **105**, 57–69.

- McDonough W. F., Stosch H.-G. and Ware N. G. (1992) Distribution of titanium and the rare earth elements between peridotitic minerals. *Contrib. Miner. Petrol.* **110**, 321–328.
- McDonough W. F. and Sun S. S. (1995) The composition of the Earth. *Chem. Geol.* **120**, 223–253.
- Meisel T., Walker R. J., Irving A. J. and Lorand J. P. (2001) Osmium isotopic compositions of mantle xenoliths: a global perspective. *Geochim. Cosmochim. Acta* **65**(8), 1311–1323.
- Meyers J., Rosendal B. R., Harrison C. G. and Ding Z. D. (1998) Deep-imaging seismic and gravity results from the offshore Cameroon Volcanic Line and speculation of African hotlines. *Tectonophysics* **284**, 31–63.
- Niu Y. L. (1997) Mantle melting and melt extraction processes beneath ocean ridges: evidence from abyssal peridotites. *J. Petrol.* **38**, 1047–1074.
- Nowell G. M., Kempton P. D., Noble S. R., Fitton J. G., Saunders A. D., Mahoney J. J. and Taylor R. N. (1998) High precision Hf isotope measurements of MORB and OIB by thermal ionisation mass spectrometry: insights into the depleted mantle. *Chem. Geol.* **149**, 211–233.
- O'Reilly S. Y. and Griffin W. L. (1988) Mantle metasomatism beneath western Victoria, Australia: I. Metasomatic processes in Cr-diopside lherzolites. *Geochim. Cosmochim. Acta* **52**, 433–447.
- Pearson D. G., Carlson R. W., Shirey S. B., Boyd F. R. and Nixon P. H. (1995) Stabilization of Archean lithospheric mantle—a Re–Os isotope study of peridotite xenoliths from the Kaapvaal Craton. *Earth Planet. Sci. Lett.* **134**, 341–357.
- Pearson D. G. and Nowell G. M. (2002) The continental lithospheric mantle reservoir: characteristics and significance as a mantle reservoir. *Proc. Royal Soc., Ser. A* **360**, 1–28.
- Pearson D. G., Irvine G. J., Ionov D. A., Boyd F. R. and Dreibus G. E. (2004) Re–Os isotope systematics and platinum group element fractionation during mantle melt extraction: a study of massif and xenolith peridotite suites. *Chem. Geol.* **208**, 29–59.
- Pearson D. G., Parman S. W. and Nowell G. M. (2007) A link between large mantle melting events and continent growth seen in osmium isotopes. *Nature* **449**, 202.
- Pearson D. G. and Wittig N. (2008) Formation of Archean continental lithosphere and its diamonds: the root of the problem. *J. Geol. Soc.* **165**, 895–914.
- Pearson D. G. and Wittig N. (2014) *3.6 – The formation and evolution of the subcontinental mantle lithosphere – evidence from mantle xenoliths*, second ed. Elsevier, Oxford, pp. 255–292.
- Penaye J., Toteu S. F., Van Schmus W. R. and Nzenti J. P. (1993) U–Pb and Sm–Nd preliminary data on the Yaoundé series, Cameroon: re-interpretation of the granulitic rocks as the suture of a collision in the ‘Centrafrican belt’. *C.R. Acad. Sci. Paris* **317**, 789–794.
- Peregoedova A., Barnes S. J. and Baker D. R. (2004) The formation of Pt–Ir alloys and Cu–Pd-rich sulfide melts by partial desulfurization of Fe–Ni–Cu sulfides: results of experiments and implications for natural systems. *Chem. Geol.* **208**, 247–264.
- Peslier A. H., Reisberg L., Ludden J. and Francis D. (2000) Os isotopic systematics inmantlexenoliths: age constraints on the Canadian Cordillera lithosphere. *Chem. Geol.* **166**(1–2), 85101.
- Pearson, D.G., Nowell, G.M., Dating mantle differentiation: a comparison of the Lu–Hf, Re–Os and Sm–Nd isotope systems in the Beni Bousera peridotite massif and constraints on the Nd–Hf composition of the lithospheric mantle. *Geophysical Research* 05430, 2003, Abstracts 5.
- Pintér Z., Patko L., Djoukam J. F. T., Kovacs I., Tchouankoue J. P., Falus G., Kone Z., Tommasi A., Barou F., Mihaly J., Nemeth C. and Jeffries T. (2015) Characterization of the sub-continental lithospheric mantle beneath the Cameroon volcanic line inferred from alkaline basalt hosted peridotite xenoliths from Barombi Mbo and Nyos Lakes. *J. Afr. Earth Sc.* **111**, 170–193.
- Princivalle F., Salviulo G., Marzoli A. and Piccirillo E. M. (2000) Clinopyroxene of spinel-peridotite mantle xenoliths from Lake Nji (Cameroon Volcanic Line W Africa): crystal chemistry and petrological implications. *Contrib. Mineral. Petrol.* **139**, 503–508.
- Rampone E., Botazzi P. and Ottolini L. (1991) Complementary Ti and Zr anomalies in orthopyroxene and clinopyroxene from mantle peridotites. *Nature* **354**, 518–520.
- Reisberg L. and Lorand J. P. (1995) Longevity of Sub-continental mantle lithosphere from osmium isotope systematics in orogenic peridotite massifs. *Nature* **376**, 159–162.
- Reusch A. M., Nyblade A. A., Wiens D. A., Shore P. J., Ateba B., Tabod C. T. and Nnange J. M. (2010) Upper mantle structure beneath Cameroon from body wave tomography and the origin of the Cameroon Volcanic Line. *Geochem. Geophys. Geosyst.* **11**, Q10W07.
- Rudnick R. L., McDonough W. F. and Chappell B. W. (1993) Carbonatite metasomatism in the northern Tanzanian mantle: petrographic and geochemical characteristics. *Earth Planet. Sci. Lett.* **114**(4), 463–475.
- Rudnick R. L. and Walker R. J. (2009) Interpreting ages from Re–Os isotopes in peridotites. *Lithos* **112S**, 1083–1095.
- Schmidberger S. S., Simonetti A., Francis D. and Gariepy C. (2002) Probing Archean lithosphere using the Lu–Hf isotope systematics of peridotite xenoliths from Somerset Island kimberlites. *Canada. Earth Planet. Sci. Lett.* **197**, 245–259.
- Scherer E. E., Cameron K. L. and Blichert-Toft J. (2000) Lu–Hf garnet geochronology: closure temperature relative to the Sm–Nd system and the effects of trace mineral inclusions. *Geochim. Cosmochim. Acta* **64**, 3413–3432.
- Shu Q., Brey G. P., Gerdes A. and Hoefer H. (2014) Mantle eclogites and garnet pyrox-enites – the meaning of two-point isochrons, Sm–Nd and Lu–Hf closure tem-perature and the cooling of the subcratonic mantle. *Earth Planet. Sci. Lett.* **389**, 143–154.
- Scott J. M., Liu J. G., Pearson D. G. and Waught T. E. (2016) Mantle depletion and metasomatism recorded in orthopyroxene in highly depleted peridotites. *Chem. Geol.* **441**, 280–291.
- Shu Q., Brey G. P., Gerdes A. and Hoefer E. H. (2013) Geochronological and geochemical constraints on the formation and evolution of the mantle underneath the Kaapvaal craton: Lu–Hf and Sm–Nd systematics of subcalcic garnets from highly depleted peridotites. *Geochim. Cosmochim. Acta* **113**, 1–20.
- Shu Q. and Brey G. P. (2015) Ancient mantle metasomatism recorded in subcalcic garnet xenocrysts: temporal links between mantle metasomatism diamond growth and crustal tectono magmatism. *Earth Planet. Sci. Lett.* **418**, 27–39.
- Stracke A., Snow J. E., Hellebrand E., von der Handt A., Bourdon B., Birbaum K. and Gunther D. (2011) Abyssal peridotite Hf isotopes identify extreme mantle depletion. *Earth Planet. Sci. Lett.* **308**, 359–368.
- Sun S.-S. and McDonough W. F. (1989) Chemical and isotopic systematics of oceanic basalts: implications for mantle composition and processes. *Geol. Soc., Lond., Special Publ.* **42**, 313–345.
- Tamen J., Nkoumbou C., Reusser E. and Tchoua F. (2015) Petrology and geochemistry of mantle xenoliths from the Kapsiki Plateau (Cameroon Volcanic Line): implications for lithospheric upwelling. *J. Afr. Earth Sc.* **101**, 119–134.
- Tanko Njiosseu E. L., Nzenti J.-P., Njanko T., Kapajika B. and Nédélec A. (2005) New U–Pb zircon ages from Tonga (Cameroon): coexisting Eburnean–Transamazonian (2.1 Ga) and Pan-African (0.6 Ga) imprints. *C.R. Geosci.* **337**, 551–562.

- Temdjam R. (2012) Ultramafic xenoliths from Lake Nyos area Cameroon volcanic line West-central Africa: petrography mineral chemistry equilibration conditions and metasomatic features. *Chem. Erde* **72**, 39–60.
- Teitchou M. L., Gregoire M., Dantas C. and Tchoua F. M. (2007) Le manteau supérieur à l'aplomb de la plaine de Kumba (ligne du Cameroun), d'après less enclaves de peridotites à spinelles dans les laves basaltiques. *Comptes Rendus Geosci.* **339**, 101–109.
- Toteu S. F., Van Schmus W. R., Penaye J. and Nyobe J. B. (1994) U-Pb and Sm–Nd evidence for Eburnian and Pan-African high-grade metamorphism in cratonic rocks of southern Cameroon. *Precamb. Res.* **67**, 321–347.
- Toteu S. F., Van Schmus R. W., Penaye J. and Michard A. (2001) New U-Pb and Sm–Nd data from north-central Cameroon and its bearing on the pre-Pan-African history of central Africa. *Precambr. Res.* **108**, 45–73.
- Toteu S. F., Penaye J. and Djomani Y. P. (2004) Geodynamic evolution of the Pan-African belt in central Africa with special reference to Cameroon. *Can. J. Earth Sci.* **41**, 73–85.
- Trompette, R., 1994. Geology of western Gondwana (2000–500 Ma) Pan-African Brazilian aggregation of South America and Africa. A.A. Balkema Rotterdam. The Netherlands.
- Vervoort J. D. and Blichert-Toft J. (1999) Evolution of the depleted mantle: Hf isotope evidence from juvenile rocks through time. *Geochim. Cosmochim. Acta* **63**, 533–556.
- Walker R. J., Shirey S. B., Hanson G. N., Rajamani V. and Horan M. F. (1989) Re–Os Rb–Sr and O isotopic systematics of the Archean Kolar schist belt Karnataka India. *Geochim. Cosmochim. Acta* **53**, 3005–3013.
- Wandji P., Tsafack J. P. F., Bardintzeff J. M., Nkouathio D. G., Dongmo A. K., Bellon H. and Guillou H. (2009) Xenoliths of dunites wehrlites and clinopyroxenites in the basanites from Batoke volcanic cone (Mount Cameroon Central Africa): petrogenetic implications. *Mineral. Petrol.* **98**, 81–98.
- Wittig N., Baker J. A. and Downes H. (2006) Dating the mantle roots of young continental crust. *Geology* **34**, 237–240.
- Yaxley G. M., Green D. H. and Kamenetsky V. (1998) Carbonatite metasomatism in the southeastern Australian lithosphere. *J. Petrol.* **39**(11–12), 1917–1930.
- Zangana N. A., Downes H., Thirlwall M. F., Marriner G. F. and Bea F. (1999) Geochemical variation in peridotite xenoliths and their constituent clinopyroxenes from Ray Pic (French Massif Central): implications for the composition of the shallow lithospheric mantle. *Chem. Geol.* **153**, 11–35.
- Zhang Y.-L., Ge W.-C., Sun J., Yang H., Liu Z.-C. and Liu J. (2019) Age and composition of the subcontinental lithospheric mantle beneath the Xing'an–Mongolia Orogenic Belt: Implications for the construction of microcontinents during accretionary orogenesis. *Lithos* **326–327**, 556–571.

Associate editor: Fang-Zhen Teng